ADVANCED MATERIALS
www.advmat.de

Morphology-Controlled Metal Sulfides and Phosphides for Electrochemical Water Splitting

Jinwhan Joo, Taekyung Kim, Jaeyoung Lee, Sang-Il Choi, and Kwangyeol Lee**

Because H_2 is considered a promising clean energy source, water electrolysis has attracted great interest in related research and technology. Noble-metal-based catalysts are used as electrode materials in water electrolyzers, but their high cost and low abundance have impeded them from being used in practical areas. Recently, metal sulfides and phosphides based on earth-abundant transition metals have emerged as promising candidates for efficient water-splitting catalysts. Most studies have focused on adjusting the composition of the metal sulfides and phosphides to enhance the catalytic performance. However, morphology control of catalysts, including faceted and hollow structures, is much less explored for these systems because of difficulties in the synthesis, which requires a deep understanding of the nanocrystal growth process. Herein, representative synthetic methods for morphology-controlled metal sulfides and phosphides are introduced to provide insights into these methodologies. The electrolytic performance of morphology-controlled metal sulfide- and phosphide-based nanocatalysts with enhanced surface area and intrinsically high catalytic activity is also summarized and the future research directions for this promising catalyst group is discussed.

1. Introduction

Massive combustion of fossil fuels poses a severe threat to the world by releasing gases that cause air pollution and global warming.[1,2] Therefore, tremendous efforts are focused on developing technologies that utilize clean and renewable energy from resources such as solar energy, geothermal energy, bioenergy, wind power, and hydropower.[3–7] Since H_2 gas is considered as a carbon-zero energy source, water electrolysis has received great interest in related research and technical fields.[8–10] The current state-of-the-art water electrolysis technology requires the use of Pt- and Ir-based electrocatalysts for the hydrogen evolution reaction (HER) at the cathode and the oxygen evolution reaction (OER) at the anode.[8,11,12] However, the high cost and low abundance of these precious metals greatly impede the widespread penetration of water electrolysis technology.[13,14]

Nanoscale metal sulfides and phosphides based on earth-abundant transition metals have recently emerged as economical alternatives to the precious metal-based water-splitting electrocatalysts.[15–20] The catalytic activity of these materials can be enhanced by adjusting their compositions.[21–24] Therefore, most studies have focused on adjusting the stoichiometry of these materials to obtain the best performance in water electrolysis. Progress on this topic has been broadly covered in several reviews.[16,25,26] However, studies on improving the water-splitting performance through morphology control of nanoscale metal sulfides and phosphides have not been fully reviewed despite their potentially great impact on catalysis. Recent studies show that morphology-controlled nanocatalysts improve the catalytic activity of various metal nanoparticles and that the same strategy can be extended to improve catalytic properties of metal sulfides and phosphides.[27–35] For example, Liu and co-workers[28] reported that highly porous CoP polyhedra with large surface areas exhibit HER and OER activities owing to the increase in the number of accessible catalytic active sites. Similarly, Yu et al.[29] showed that the hollow CoP nanocatalyst loaded on N-doped graphene (CoP_h/NG) has higher electrolysis activity than solid CoP_s/NG in alkaline conditions for HER and OER. Recently, Feng et al.[33] reported that the Ni_3S_2 nanocatalyst enclosed by high index facets of $\{\bar{2}10\}$ can function as a highly active and stable electrocatalyst for water splitting because these facets can promote the adsorption of reactive intermediates on the surfaces. In addition to the earth-abundant metal sulfides and phosphides, nanostructures of noble metal sulfides and phosphides with outstanding performance have been also investigated recently.[36–41] For instance, Duan et al.[36] showed that Rh_2P nanocubes have superb HER and OER activities due to the exposure of P-rich faces and defects on the catalyst surfaces. Wang et al.[37] reported that Rh_2P nanosheets have a capability of boosting the HER performance at the universal pH conditions due to their novel thin wrinkle structures. Therefore, it is evident that the catalytic activity of noble metal sulfides and phosphides in electrolysis can also benefit from morphology-controlled nanostructure.

J. Joo, T. Kim, J. Lee, Prof. K. Lee
Department of Chemistry
Korea University
Seoul 02841, South Korea
E-mail: kylee1@korea.ac.kr
Prof. S.-I. Choi
Department of Chemistry and Green-Nano Materials Research Center
Kyungpook National University
Daegu 41566, Republic of Korea
E-mail: sichoi@knu.ac.kr
The ORCID identification number(s) for the author(s) of this article can be found under https://doi.org/10.1002/adma.201806682.

DOI: 10.1002/adma.201806682

To highlight the importance of recent developments, we herein review metal-sulfide- and metal-phosphide-based nanocatalysts with enhanced surface area and intrinsically high catalytic activity by controlling the facets and making hollow structures. We first provide the mechanisms of water-splitting reactions and the roles of S and P atoms in metal sulfides and phosphides for catalysis. Then, we discuss the representative synthetic methods to obtain hollow and facet-controlled nanocatalysts. Next, the relationship between morphology-controlled nanostructures and their electrolytic performance is discussed based on various experimental and theoretical evaluation data. Finally, we provide an outlook to shed light on fruitful directions for future research on these materials.

2. Role of S and P Atoms in Metal Sulfides and Phosphides for Water Splitting

2.1. General Mechanisms of the HER and OER

As shown in **Figure 1**a, electrocatalytic water splitting consists of two half-cell reactions, namely, HER and OER, which involve proton or water reduction occurring at the cathode and water or hydroxide oxidation at the anode, respectively,[19,42–49] and can be written as follows

$$\text{Total reaction: } 2H_2O \rightarrow 2H_2 + O_2 \tag{1}$$

Acidic condition

$$\text{Cathode: } 2H^+ + 2e^- \rightarrow H_2,\ E_c = 0\ \text{V}$$
$$\text{Anode: } 2H_2O \rightarrow O_2 + 4H^+ + 4e^-,\ E_a = 1.23\ \text{V} \tag{2}$$

Alkaline condition

$$\text{Cathode: } 2H_2O + 2e^- \rightarrow H_2 + 2OH^-,\ E_c = -0.83\ \text{V}$$
$$\text{Anode: } 4OH^- \rightarrow O_2 + 2H_2O + 4e^-,\ E_a = -0.40\ \text{V} \tag{3}$$

The theoretical thermodynamic potential of overall water splitting is 1.23 V in both acidic and alkaline electrolytes at 25 °C and 1 atm. However, more potential must be applied to electrolysis in actual operations. This excess potential (known as overpotential, η) is caused by resistances among electrodes, the catalyst, and the electrolyte.

As investigated in recent studies, HER in acidic electrolytes is more active because the reduction of a proton is energetically more favorable than that of a neutral water molecule in alkaline electrolytes.[50] The HER mechanism is usually revealed by the experimentally obtained Tafel slope values.[51–53] In general, the HER reaction mechanism consists of three reaction steps:[48] the first step is known as the Volmer step ($H^+ + e^- \rightarrow H_{ads}$), which involves discharging protons on the surface of electrode to form adsorbed hydrogen, H_{ads}. After producing H_{ads}, two steps, the Heyrovsky ($H_{ads} + H^+ + e^- \rightarrow H_2$) and relatively fast Tafel ($H_{ads} + H_{ads} \rightarrow H_2$), proceed competitively or together for H_2 evolution. When the coverage of H_{ads} on the catalyst surface is relatively low, sequential Volmer and Heyrovsky steps occur dominantly (left route in Figure 1b). However, the faster Volmer–Tafel steps will take place under sufficient coverage of high H_{ads} on the catalyst (right route in Figure 1b). In alkaline conditions, the HER is sluggish compared to that in acidic conditions because of water dissociation prior to the formation of H_{ads}.

Irrespective of the reaction conditions, the H_{ads} on the cathode is always involved in the HER. Therefore, to evaluate the HER activity of catalysts, it is important to estimate the differential adsorption energy of H (ΔE_H) that describes the bond strength between H and the active site atom[54] and the free energy of H_{ads} (ΔG_H), which is widely accepted as a marker for hydrogen evolution performance. If ΔG_H is a large negative value, hydrogen adsorption takes place easily and hydrogen is bound strongly on the electrode. On the other hand, if ΔG_H is a large positive value, the hydrogen will be weakly bound with the electrode, which shows the slow Volmer step. Therefore, the value of ΔG_H near zero is usually considered as the indicator for good HER catalysts.

In the case of the OER, Matsumoto and Sato[45] reviewed some possible OER mechanisms in acid and alkaline media proposed by many research groups[55–60] (**Table 1**). The most frequently accepted mechanisms in acidic conditions are the oxide path and

Sang-Il Choi received his Ph.D. degree in inorganic chemistry from KAIST (2011). After his postdoctoral research in the Xia group at the Georgia Institute of Technology, USA, he joined the Kyungpook National University in 2015 as an assistant professor. His research interests include design and synthesis of nanomaterials and exploration of their applications in electrocatalysis.

Kwangyeol Lee obtained his Ph.D. degree (1997) in chemistry from the University of Illinois at Urbana–Champaign. After fulfilling his military obligation, he joined Korea University in 2003 as a chemistry faculty member, before being appointed as a professor. His current interests include the development of synthetic methodologies for nanoscale materials, the application of nanomaterials in biomedical fields, and the development of nanotechnologies to support the environment by creating sustainable energy sources.

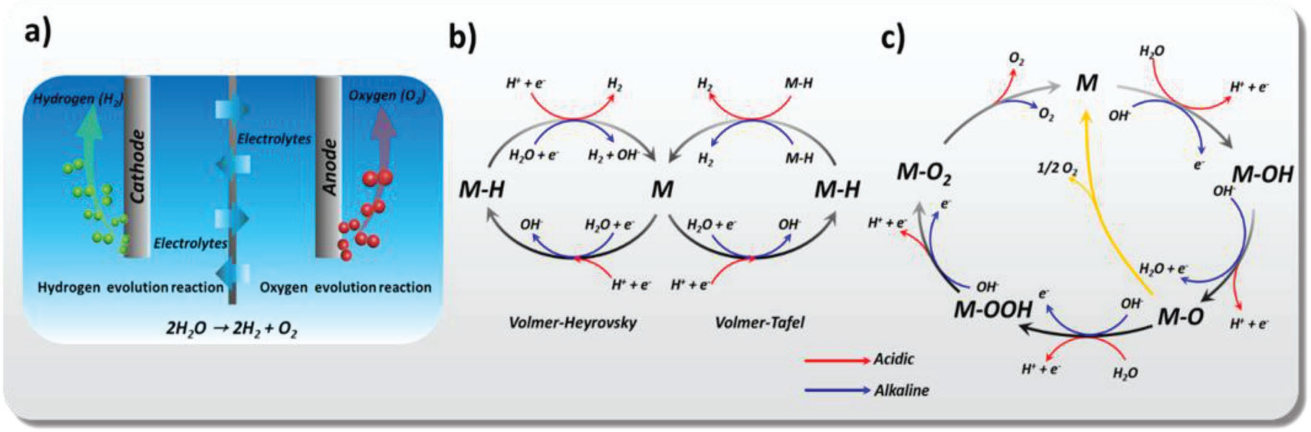

Figure 1. a) Schematic illustration of an electrolyzer. b,c) General reaction pathways for the hydrogen evolution reaction and oxygen evolution reaction, respectively.

electrochemical oxide path. In the alkaline condition, all of the mechanisms exhibit M–OH formation steps in the initial stage via attachment of hydroxide ions at the active site, followed by other intermediate formations. There are similarities among the proposed OER mechanisms in that most of the proposed mechanisms show intermediates such as M–O and M–OH regardless of the electrolyte conditions. However, the oxygen evolution step can be divided into two categories: the direct oxygen-evolving step from the M–O intermediate, as indicated by yellow arrows in Figure 1c, and the formation of the M–OOH route that subsequently produces M–O_2. Reflecting the aforementioned reaction steps, the widely accepted reaction pathways for the OER are illustrated in Figure 1c.

As shown in Table 1, the OER mechanisms have complex multistage. These mechanisms require considerably large overpotentials to accomplish the overall reaction because the kinetic barrier of the elementary steps must be overcome. One of the elementary reaction steps with the highest kinetic barrier is regarded as the rate-determining step (RDS), and many pioneering researchers[55,56,61] have utilized the Tafel slope, b, defined by the equation below, in order to obtain important insights into the mechanistic pathway for the OER

$$b = \mathrm{d}\log i/\mathrm{d}\eta = (2.303\ RT)/(\alpha_a F) \quad (4)$$

where η is the overpotential, R is the ideal gas constant, T is the absolute temperature, F is the Faraday constant, and α_a is the transfer coefficient for the anodic reaction. In particular, α_a can be given as follows for a multistage reaction like OER

$$\alpha_a = \left(n_f/\nu + n_r\beta\right) \quad (5)$$

where n_f is the number of electrons transferred before RDS, ν is the stoichiometric factor defined as the number of times the RDS occurs for the overall reaction, n_r is the number of electrons transferred in each occurrence of the RDS, and β is the symmetry factor. In general, n_r, ν, and α_a are accepted

Table 1. The oxygen evolution mechanisms summarized by Matsumoto and Sato. Reproduced with permission.[45] Copyright 1986, Elsevier.

Acidic condition	Alkaline condition
Electrochemical oxide path[55]	**Electrochemical oxide path**[55]
M[a)] + $H_2O \rightarrow$ MOH + $H^+ + e^-$	M + $OH^- \rightarrow$ M—OH + e^-
MOH $\rightarrow$ MO + $H^+ + e^-$	M—OH + $OH^- \rightarrow$ M—O + $H_2O + e^-$
M—O + M—O $\rightarrow$ 2M + O_2	M—O + M—O $\rightarrow$ 2M + O_2
Oxide path[55]	**Oxide path**[55]
M + $H_2O \rightarrow$ M—OH + $H^+ + e^-$	M + $OH^- \rightarrow$ M—OH + e^-
M—OH + M—OH $\rightarrow$ M—O + H_2O + M	M—OH + M—OH $\rightarrow$ M—O + H_2O + M
M—O + M—O $\rightarrow$ 2M + O_2	M—O + M—O $\rightarrow$ 2M + O_2
Krasil'shchkov path[56]	**Krasil'shchkov path**[56]
M + $H_2O \rightarrow$ M—OH + $H^+ + e^-$	M + $OH^- \rightarrow$ M—OH + e^-
M—OH $\rightarrow$ M—O^- + H^+	M—OH + $OH^- \rightarrow$ M—O^- + H_2O
M—O^- $\rightarrow$ M—O + e^-	M—O^- $\rightarrow$ M—O + e^-
M—O + M—O $\rightarrow$ 2M + O_2	M—O + M—O $\rightarrow$ 2M + O_2
Wade and Hackerman's path[57]	**Yeager's path**[58,59]
2M + $2H_2O \rightarrow$ M—O + M—H_2O + $2H^+ + 2e^-$	M + $OH^- \rightarrow$ M—OH + e^-
M—O + 2M—$OH^- \rightarrow$ 2M + M—H_2O + O_2 + $2e^-$	M^z—OH $\rightarrow$ M^{z+1}—OH + e^-
	$2M^{z+1}$—OH + $2OH^- \rightarrow$ 2M + $2H_2O$ + O_2
	Bockris path[60]
	M + $OH^- \rightarrow$ M—OH + e^-
	M—OH + $OH^- \rightarrow$ M–H_2O_2 + e^-
	M—H_2O_2 + $OH^- \rightarrow$ M—OOH^- + H_2O
	M—H_2O_2 + M—$OOH^- \rightarrow$ H_2O + OH^- + O_2

[a)]M means a surface active site.

as 1, 1, and 0.5, respectively, for a multistage reaction with a single RDS.[62] Thus, for example, if the first reaction step, ($M + H_2O \rightarrow M–OH + H^+ + e^-$), in OER is the RDS (Figure 1c), the Tafel slope will be 120 mV decade^{-1} because $n_f = 0$. However, if the second step, ($M–OH \rightarrow M–O + H^+ + e^-$), is the RDS, the Tafel slope will be 40 mV decade^{-1} with the parameters of $n_f = 1$ and $\alpha_a = 1.5$. In this manner, the RDS of the OER can be determined by the measured Tafel slope, and hence, the reaction mechanism can be understood.

Recently, the density function theory (DFT) calculation method was applied to the OER in order to understand the thermodynamics in each reaction step by Rossmeisl et al.[63] In their work, they considered four reaction steps for a model reaction mechanism

$$2H_2O + M \rightarrow H_2O + M–OH + H^+ + e^- \quad (6)$$

$$\Delta G_1 = \Delta G_{M–OH} - \Delta G_{H_2O} - eU + k_B T \ln\left[H^+\right]$$

$$H_2O + M–OH \rightarrow H_2O + M–O + H^+ + e^- \quad (7)$$

$$\Delta G_2 = \Delta G_{M–O} - \Delta G_{M–OH} - eU + k_B T \ln\left[H^+\right]$$

$$H_2O + M–O \rightarrow M–OOH + H^+ + e^- \quad (8)$$

$$\Delta G_3 = \Delta G_{M–OOH} - \Delta G_{M–O} - eU + k_B T \ln\left[H^+\right]$$

$$M–OOH \rightarrow M + O_2 + H^+ + e^- \quad (9)$$

$$\Delta G_4 = \Delta G_{O_2} - \Delta G_{M–OOH} - eU + k_B T \ln\left[H^+\right]$$

where ΔG_i (i = 1, 2, 3, 4) is the Gibbs free energy of the ith reaction step, U is the electrode potential versus the standard hydrogen electrode (SHE), and k_B is the Boltzmann constant. As shown in the above equations, the reaction energy for each step was defined as the difference between two adsorbed intermediates; for example, ΔG of reaction step 2 (ΔG_2) is described as the Gibbs free energy difference between M–O ($\Delta G_{M–O}$) and M–OH ($\Delta G_{M–OH}$). The rest of ΔG_i can be obtained with the same logic, and the step with the largest value among them is defined as the potential-determining step (PDS) or ΔG for OER (ΔG^{OER}). The magnitude of ΔG^{OER} is given as[62,63]

$$\Delta G^{OER} = \max\{\Delta G_1, \Delta G_2, \Delta G_3, \Delta G_4\} \quad (10)$$

The relationship between ΔG^{OER} and theoretical overpotential (η^{OER}) under standard conditions with $U = 0$ versus SHE is given as

$$\eta^{OER} = (\Delta G^{OER}/e) - 1.23\ \text{V} \quad (11)$$

Man et al.[42] showed that the ideal value of ΔG^{OER} is 1.23 eV when η^{OER} is zero, indicating that all the values of ΔG_1, ΔG_2, ΔG_3, and ΔG_4 are equal to 1.23 eV. Thus, the ideal OER catalyst has equal adsorption energies for the elementary reaction steps. In other words, all the elementary reaction steps can be thermodynamically favorable steps. Moreover, according to the comparison works of real and ideal catalysts,[64] M–OOH intermediates bind weakly on the surface active site of a real catalyst.

In brief, the Tafel slope and ΔG^{OER} analyses can provide complementary insights for understanding the OER mechanism; the Tafel slope analysis is capable of providing kinetic information of catalysts for the OER, while ΔG^{OER} is capable of affording thermodynamic information between the intermediates and the catalysts.

2.2. Insights into the Role of S and P Atoms in the HER

Understanding the role of S and P atoms in metal sulfides and phosphides is crucial to the development of a rational synthetic route to electrocatalysts toward efficient water splitting. Recently, Shi and Zhang[53] have summarized the effect of P on HER activity. According to their work, P atoms in metal phosphides can draw the electron from the metal because of their high electronegativity. Thus, negatively charged P atoms can trap the positively charged proton like a base. For this reason, metal phosphides with an increased relative P content usually showed improvement in the HER performance. Accordingly, as shown in **Figure 2**a, which compares the HER activity of $Ni_{12}P_5$, Ni_2P, and Ni_5P_4, nickel phosphides with higher P contents exhibited higher activity.[65] A similar result was also found in the works of Callejas et al.,[66] in which CoP showed better activity than Co_2P (Figure 2b). A similar logic was applied to S atoms in metal sulfides by Anantharj et al.[26] On the one hand, they claimed that S atoms on the surface of metal sulfides act as a site for the attachment and detachment of H atom similar to P atoms of metal phosphides. On the other hand, they expressed concerns for the possibility of decreasing the HER activity because S atoms are more electronegative than P atoms; therefore, the relatively higher bond strength between S and H can cause poor efficiency of HER.

As mentioned in Section 2.1, ΔG_H can be a good descriptor to judge the activity of the HER catalyst, and catalysts with near-zero values of ΔG_H have the ability to attach and detach hydrogen efficiently on the surface of catalytic sites. Occasionally, direct comparison of the bond strength, ΔE_H, between H_{ads} and the active-site atom is also used. Liu and Rodriguez reported the DFT calculation result that Ni_2P (001) is anticipated to exhibit outstanding HER activity.[67] According to their results, negatively charged P atoms on the (001) facet of Ni_2P can not only serve as proton acceptors, but also promote hydrogen desorption. As shown in Figure 2c, the first adsorption energy of H, ΔE_{H1}, is –0.54 eV at the hollow Ni site, but the addition of the second H at the P–Ni bridge site can make the bond strength of H, ΔE_{H2}, weaker by as much as 0.09 eV compared to ΔE_{H1}. Therefore, they claimed that this decreased bond strength could lower the H_2 desorption energy and promote the HER activity. Further detailed DFT calculations comparing ΔG_H of Mo to MoP at the active sites, acquired by Xiao et al., show that the P atoms play an important role in the HER. Their works indicated that ΔG_H of the P atoms on the surface of MoP was negative enough to promote hydrogen adsorption with low H coverage (–0.36 and –0.03 eV at 1/4 ML (monolayer) and 2/4 ML coverage; Figure 2d).[68] On the other hand, when H coverage was increased to more than 3/4ML, ΔG_H became positive (0.34 eV). This result

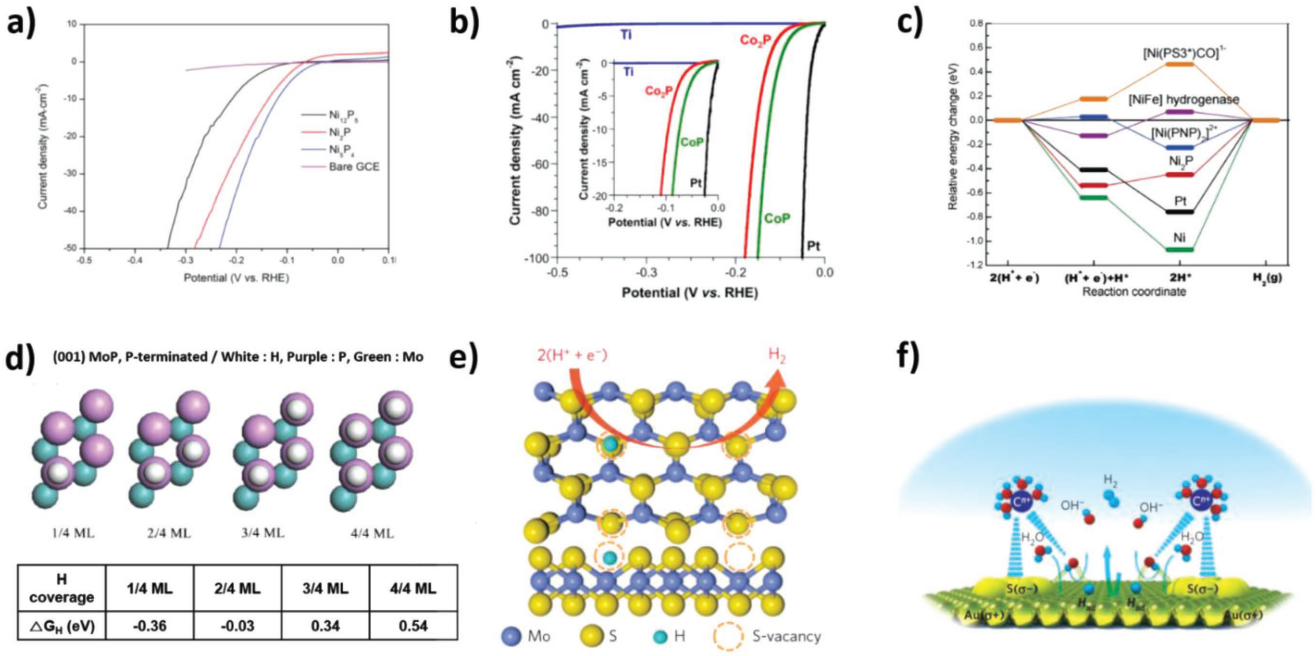

H coverage	1/4 ML	2/4 ML	3/4 ML	4/4 ML
$\triangle G_H$ (eV)	-0.36	-0.03	0.34	0.54

Figure 2. a) LSV curves of bare GCE, $Ni_{12}P5$, Ni_2P, and Ni_5P_4 NCs in 0.5 M H_2SO_4. Reproduced with permission.[65] Copyright 2015, The Royal Society of Chemistry. b) Polarization data (plots of current density vs potential) in 0.5 M H_2SO_4 for Co_2P/Ti and CoP/Ti electrodes. Reproduced with permission.[66] Copyright 2015, American Chemical Society. c) Calculated relative energy changes for the HER on the Ni_2P(001), Pt(111), and Ni(111) surfaces. Reproduced with permission.[67] Copyright 2005, American Chemical Society. d) Calculated binding energy and Gibbs free energy of H adsorption on (001) MoP, P terminated surfaces. Reproduced with permission.[68] Copyright 2014, The Royal Society of Chemistry. e) Schematic modeling of the top (upper panel) and edge (low panel) views of MoS_2 with S-vacancies. Reproduced with permission.[69] Copyright 2015, Springer Nature. f) Schematic illustration of the effect of $S^{\delta-}$ induced stabilization of hydrated cations that promote water dissociation. Reproduced with permission.[73] Copyright 2015, Springer Nature.

shows that P of MoP prefers H adsorption at low H coverage but desorption at high coverage. Thus, they could conclude that MoP possesses better performance than Mo in the HER because P atoms behave like a hydrogen deliverer.

In the case of metal sulfides, MoS_2 and WS_2 are the most spotlighted HER electrocatalysts owing to the high performance originating from their distinctive structural features. For example, the exposed S sites on the edge of a 1T-MoS_2 unit cell are known to be the active sites for HER. Likewise, the S vacancies (Figure 2e)[69] on its edge contribute to the improvement of electrocatalytic HER performance.[25,70–72] In particular, Jaramillo et al.[11] showed that the S edge of MoS_2 is an active site for the HER experimentally and theoretically. From their DFT calculations, ΔG_H of S-edge in MoS_2 is a small positive value at low H coverage (1/4ML), which means that adsorption and desorption may be favored on that site, and thus, one in four edge atoms evolves H_2 under electrolysis operation. More concrete studies about the role of S atom in the transition metal sulfides (TMS_X) for the HER has been carried out by Staszak-Jirkovsky et al.[73] Based on their experimental results, they proposed that, in alkaline conditions, S atoms with cation of transition metal has the effect to construct $S^{\delta-}$–TM^{n+}–H_2O (TM^{n+}: transition metal cation) network where the hydrated TM^{n+} enhances the water-splitting process (Figure 2f). Therefore, unlike P atoms, S atoms seem to play an indirect role in the HER, by making S-vacancies in the MoS_2 or by promoting water dissociation via the $S^{\delta-}$–TM^{n+}–H_2O network rather than by functioning as inefficient adsorption and desorption active sites.

2.3. Insights into the Role of S and P Atoms in the OER

According to Subbaraman et al.,[74] the electrocatalytic OER activities of 3d M^{2+} ions (Fe, Co, and Ni) with oxide environments tend to be increased when the OH_{ad}–M^{2+} interaction is weakened. This is mainly attributed to the increased 3d–2p repulsion between the metal d-band center and the coordinated oxygen p-band centers. In the case of metal sulfides and phosphides, electronegative S and P atoms located near the metal atoms result in the repulsion between 3p orbital of these heteroatoms and 2p orbital of oxygen, leading to the obstruction of –OH coordination on metal sulfides and phosphides and thus the OER. In this regard, metal sulfides and phosphides are not promising OER catalysts. Nevertheless, the formation of –OOH intermediates from the coordinated OH can be encouraged by the delocalized electrons among the attached oxygen, metal center, and the electronegative S and P atoms. Subsequently, the repulsive 3p–2p site accelerates the oxidation of the –OOH intermediate.

There have been many efforts to reveal the role of S and P atoms in catalysis and the true catalytically active species. Chen et al.[75] revealed that Co oxides layer, formed by in situ electrochemical treatment on cobalt sulfides, are the real active sites. In this case, cobalt sulfides function as precatalysts to produce catalytically active species for the OER. They conducted X-ray photon spectroscopy (XPS) experiment to determine the binding energy of Co oxidation state and the X-ray powder diffraction (XRD) results to show the formation of cobalt oxide.

Mabayoje et al.[76] explained that the highly improved OER activity is achieved on amorphous NiO_x, derived easily from NiS but not from pristine NiO. XPS measurements showed that binding energy of Ni 3p region shifts to higher oxidation state than that of Ni(II), revealing the Ni vacancy sites are OER active. Moreover, the formation of the oxide layers on NiS increases the electrochemically active surface area (ECSA), inducing the improvement of the OER activity (**Figure 3**a).

Metal phosphides have lately taken the center stage as a promising new class for the OER catalysts and behaved similarly as metal sulfides under OER condition, forming the oxide layers during the reaction.[77–79] In brief, P atoms of metal phosphides and S atoms of metal sulfides are considered to act alike in the OER catalysis.[26] In order to clarify and leverage the role of metal phosphides in the OER, DFT calculations of the surface energy are generally required. Unfortunately, the diversity of catalytically active species such as oxide, hydroxide, and phosphate layers formed on the surface of metal phosphides makes it very difficult to conduct precise DFT calculations. However, the highly advanced analytical techniques enable us to study the true electrocatalytically active species on the catalyst surfaces which are formed during the catalyst activation. For example, Ryu et al.[77] discovered that the OER activity of the CoP nanoparticles was actually derived from cobalt-oxo/hydroxo units abundant in phosphate species generated during the OER. As shown in Figure 3, they investigated the surface of CoP nanoparticles to determine the composition and structure of local layer which functions as effective electrocatalytic species, by using XPS, X-ray absorption near-edge spectroscopy (XANES), and extended X-ray absorption fine structures (EXAFS). In their works, they found that Co and P were transformed into oxidized species, i.e., PO_3^-(metaphosphate) from the XPS analysis (Figure 3b). In addition, the XANES peak shift to higher energy states is consistent with the XPS analysis. Thus, the newly formed species on CoP/C catalyst were revealed as cobalt metaphosphate and oxo/hydroxo units. By conducting the EXAFS technique, it was disclosed that this oxidized layer had been formed during the OER (Figure 3c). Similarly, Stern et al.[78] showed that in situ formed nickel oxide in a core–shell Ni_2P/NiO_x could function as the efficient OER electrocatalyst during the study of Ni_2P. They also analyzed the surface of Ni_2P/NiO_x particles by combination of the various analytical techniques, such as high-resolution TEM (HRTEM), energy dispersive X-ray spectroscopy (EDS) elemental mapping, and high-resolution depth-profiling XPS (Figure 3d). Moreover, according to the study of Co_2P–CoO_x by Dutta et al.,[79] P atoms at the oxide and metal phosphide interface could enhance the catalytic activity by helping the carrier transportation between core materials and oxides.

3. Synthetic Methods for Hollow Metal Sulfide and Phosphide Nanostructures

Hollow nanostructures have attracted a great research interest in the field of electrochemical energy storage and conversion owing to their unique structural features such as large surface-to-volume ratio, fast charge transfer, and beneficial mass diffusion.[22,27–30] In this section, two synthetic strategies for hollow metal sulfide and phosphide nanostructures are discussed, along with the utilization of the Kirkendall effect to the solid metal nanoparticles and the postsynthetic etching of core–shell nanoparticles.

3.1. Kirkendall Effect

The most widespread approach to obtain hollow metal sulfides and phosphides is the utilization of the Kirkendall effect during the synthesis.[29–31,65,80–86] Different diffusion rates of heterogeneous atoms at the interfaces drive this effect spontaneously. Among various examples of the Kirkendall effect,

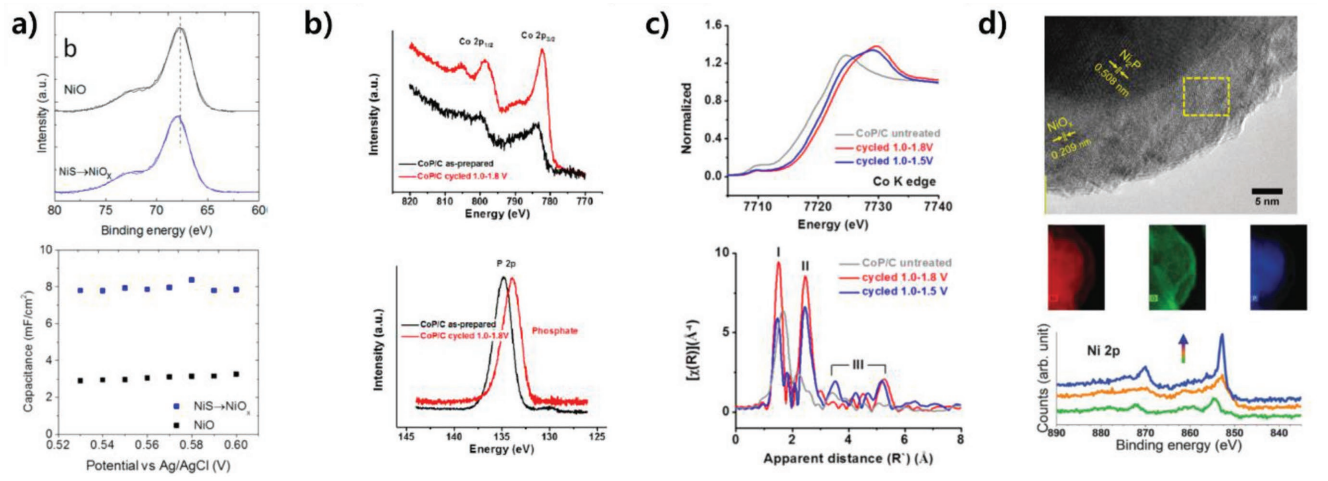

Figure 3. a) Ni 3p XPS regions comparing NiS derived NiO_x samples with NiO samples grown by thermal annealing (top) and capacitance values for NiS and NiO samples obtained through AC impedance measurements (bottom). Reproduced with permission.[76] Copyright 2016, American Chemical Society. b) Co 2p (top) and P 2p (bottom) XPS spectra, c) XANES profiles (top) and EXAFS spectra (bottom) of CoP/C before and after potential cycling. b,c) Reproduced with permission.[77] Copyright 2015, American Chemical Society. d) HRTEM (top), EDS elemental mapping (middle), and high-resolution depth-profiling XPS (bottom) of Ni_2P/NiO_x. Reproduced with permission.[78] Copyright 2015, The Royal Society of Chemistry.

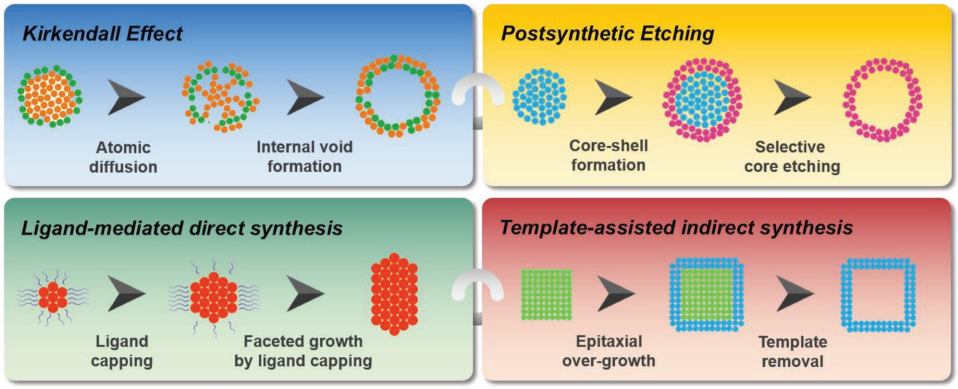

Figure 4. Representative schematic diagram of synthetic methodologies to morphology controlled nanostructures.

faster outward diffusion of metal atoms positioned at core, in conjunction with slower inward movement of S and P atoms, can lead to the production of hollow metal sulfides and phosphides. Multiple small voids at core, which appear in the early stage, coalesce into a large void of hollow structures during the process (**Figure 4**). Yin et al.[80] first reported the nanoscale Kirkendall effect on hollow cobalt sulfide nanoparticles, which were transformed from solid Co nanoparticles (**Figure 5**a). A two-step synthetic approach was utilized for synthesis of hollow cobalt sulfide nanoparticles, which show two mixed phases of cobalt sulfides including linnaeite (Co_3S_4) and cobalt pentlandite (Co_9S_8). The ratio between Co_3S_4 and Co_9S_8 phases depends on the amounts of cobalt and sulfur precursors used in the sulfidation reaction. The cavity volume in the cobalt sulfide nanoparticles ranges between 40% and 70% of the volume of the initial cobalt nanoparticles. The cavity size is inversely proportional to the concentration of sulfur precursor, and this result indicates that significant amounts of sulfur migrate inward. You et al.[81] demonstrated that hollow cobalt sulfide nanoprisms could be generated by adding sulfur thioacetamide in the solution containing presynthesized cobalt hydroxide nanoprisms. This two-step reaction is feasible by two distinct synthetic routes, namely, the microwave and solvothermal methods. Interestingly, the hollow cobalt sulfide nanoprisms synthesized by the microwave method have larger specific surface area and pore size than the counterpart obtained by solvothermal method. The Kirkendall effect could be utilized with other transition metals. For example, polycrystalline hollow spheres composed of α-NiS were synthesized by hydrothermal decomposition of a nickel precursor to form spherical Ni–organic complex clusters and subsequent reaction with S sources such as glutathione and thiourea.[30] The Ni atoms in an amorphous spherical core gradually moved to the surface and formed stable and crystalline α-NiS shell, demonstrating the hollowing process of solid particle through the Kirkendall effect. The wide investigation of the Kirkendall effect in transition metals is tightly coupled with extremely slow transport rate of sulfur.[87] Zhang et al. confirmed the diffusion rates of Co, O, and S in the anion exchange reaction with CoO by DFT calculation. According to the calculation, the diffusion activation barrier of sulfur (5.71 eV) through the CoO crystal is much larger than that of cobalt (1.14 eV). Based on these calculated barriers, cobalt diffuses critically faster than sulfur, which can explain the Kirkendall effect during the sulfidation.

In the synthesis of hollow metal phosphides, slow diffusion rate of phosphorous can cause the Kirkendall effect. Popczun et al.[31] obtained hollow CoP nanoparticles by utilizing trioctylphosphine (TOP) as the source of phosphorous in the mixture of Co nanoparticles, octadecene, and oleylamine. More recently, similar ingredients were employed for the synthesis of hollow $Ni_{12}P_5$ nanoparticles.[65] In this study, the electronegative P atoms of TOP could adsorb onto the Ni nanoparticles, which are nucleated by oleylamine. Thermal energy provided from high temperature above 300 °C breaks the P—C bond of Ni–TOP complexes and facilitates the diffusion of P atoms into the nanoparticles, resulting in the formation of hollow $Ni_{12}P_5$ nanoparticles (Figure 5b). Furthermore, the ratio of Ni to P has a great influence on the formation of hollow structure and crystal structure. In addition to hollow structures obtained from as-prepared or in situ template comprising single metal species, the reaction between multimetallic templates and precursors that supply S and P atoms could drive the evolution of solid nanoparticles to hollow ones with gradient alloy compositions due to differences in metal atom migrations.

3.2. Postsynthetic Etching

The other approach to obtain hollow metal sulfides and phosphides is removing a core from core–shell nanostructure whose shell consists of metal sulfide or phosphide. Generally, one-step and multistep reactions are introduced for the synthesis of core–shell structure. One-step reaction utilizes the different formation kinetics between core and shell materials that induce premature formation of the core and subsequent shell growth. Although the one-step reaction might be convenient, controlling the reaction kinetics of multiple precursors is not a light matter. In contrast, a multistep reaction, consisting of two or more synthesis and collection steps, can fine-tune the composition and shell thickness of core–shell structure. In the cases of metal sulfide and phosphide, most of the core–shell structures were obtained via multistep reaction because of the highly active nature of sulfur and phosphorous precursors during the synthesis, which renders the one-step process highly uncontrollable. The selective etching of core material from the core–shell nanoparticle results in the hollow structure.

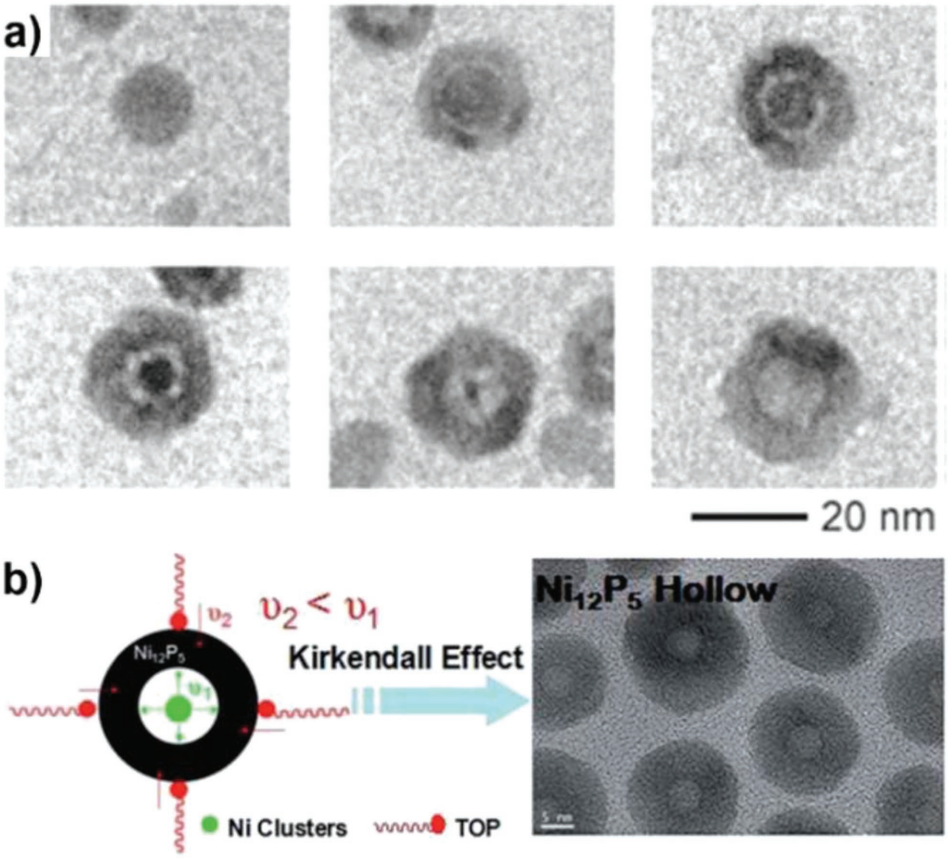

Figure 5. a) TEM images of the hollowing process of cobalt sulfide by the Kirkendall effect. Reproduced with permission.[80] Copyright 2004, The American Association for the Advancement of Science. b) Schematic image of the formation mechanism of $Ni_{12}P_5$ hollow nanoparticles through the Kirkendall effect and their TEM image. Reproduced with permission.[65] Copyright 2015, The Royal Society of Chemistry.

There are widely used templates for postsynthetic etching of core–shell structures, such as metallic oxide,[88] metal sulfide,[89] and metal–organic framework (MOF).[22,27,90–95] Kim et al.[88] reported hollow $Co_xNi_yS_z$ octahedral nanocages synthesized through sulfidation of presynthesized octahedral nanoparticles of cobalt oxide, subsequent chemical etching of remaining cobalt oxide, and cationic exchange of Co with Ni. By increasing the amount of Ni precursor, the phase changes from Co_9S_8 to Ni_3S_2/β-NiS. Zeolitic imidazolate frameworks (ZIFs) have recently emerged as a template to form hollow metal phosphides. He et al.[95] developed NiCoP/C nanoboxes through the phosphorization of as-prepared hollow ZIF-67@LDHs, which possess Ni–Co-layered double hydroxide on ZIF-67 nanocubes. A Ni precursor, added into a solution containing ZIF-67 nanocubes, infused Ni into the nanocubes and rendered them to become a hollow nanobox structure because protons, which etch the center of the nanocubes, are released by hydrolyzing Ni^{2+} ions (**Figure 6**). In another case, pyrolysis allowed ZIF-8@ZIF-67 core–shell structures to transform into hollow Co metal and N-doped carbon composition, which can be oxidized and then phosphorized to yield CoP hollow polyhedron/N-doped carbon nanotube.[28] Core–shell nanoparticles based on a metastable copper sulfide ($Cu_{2-x}S$) core, in particular, have been useful for the formation of hollow metal sulfide nanostructures. For instance, Xu et al.[89] prepared Cu_7S_4 nanoparticles to leverage as sacrificial templates for the formation of Cu_7S_4@MoS_2 via a two-step method. The injection of a mixture of the Mo and S precursors into a hot solution of presynthesized Cu_7S_4 nanoparticles allowed the growth of MoS_2 layers on the Cu_7S_4 (**Figure 7**). Then, the metastable Cu_7S_4 was dissolved in harsh reaction condition, without requiring further etching, to result in hollow MoS_2 structure. However, small amounts of Cu_7S_4 remained and these residue templates played a key role in maintaining the hollow structure. Furthermore, without the Cu_7S_4 template, bulk MoS_2 sheets were formed and showed much lower HER activity than the hollow structure of MoS_2.

In order to further increase the surface area, multilayered shells and open framework architectures can be combined with the hollow structure.[81,96–99] By utilizing novel synthetic methods, such as multistep thermal treatment of template materials followed by postsynthetic etching and phosphorization or sulfidation, dramatic changes from simple and single layer hollow structure to diverse and multishell structure can be realized.

4. Synthetic Methods for Facet-Controlled Metal Sulfides and Phosphides

Conventionally, facet-controlled nanoparticles have been prepared by the ligand-mediated method and template-assisted

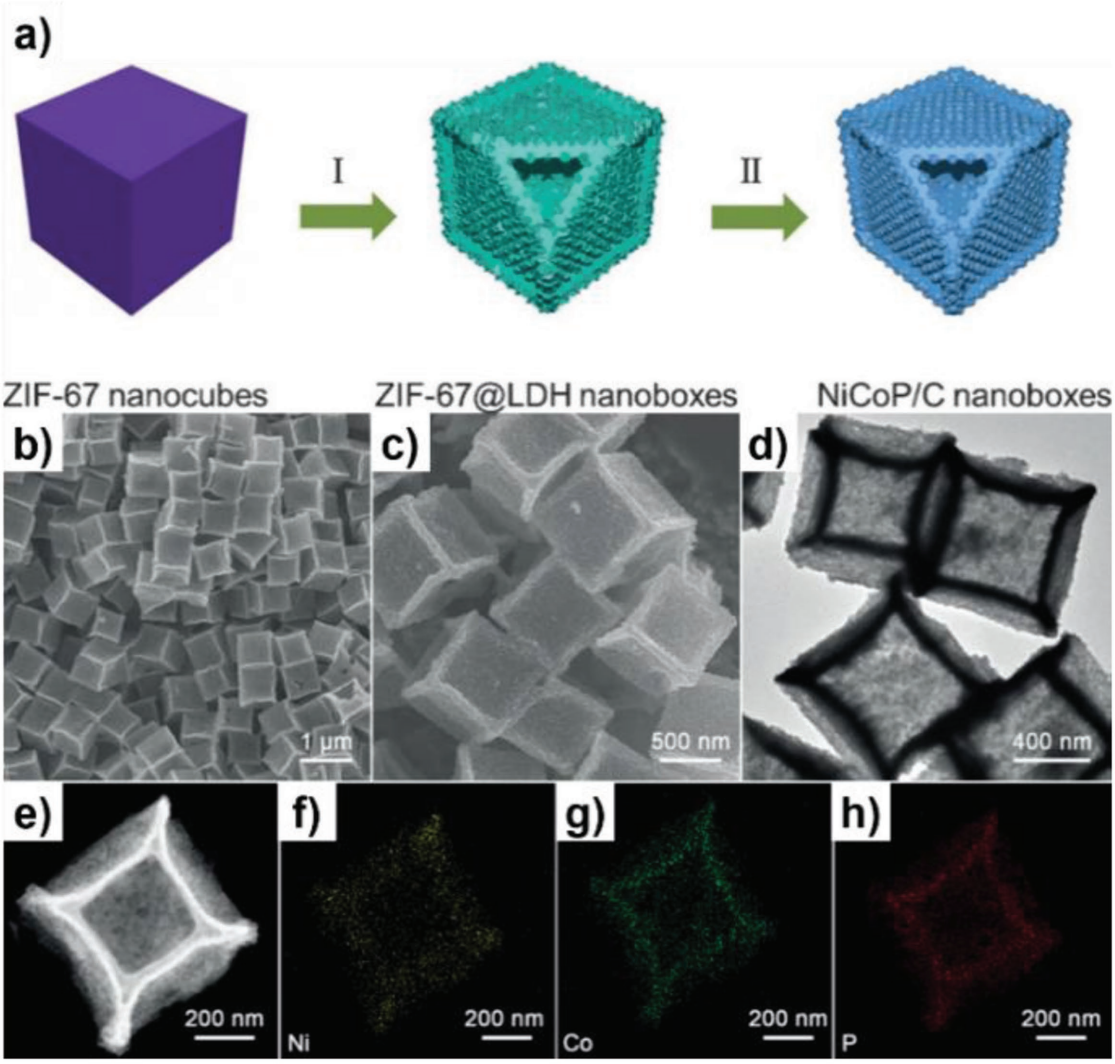

Figure 6. a) Schematic image of the reaction steps to synthesize NiCoP/C nanoboxes. b,c) SEM images, d) TEM image, and e,f) HAADF-STEM and EDS mapping of NiCoP/C nanoboxes. a–f) Reproduced with permission.[95] Copyright 2017, Wiley-VCH.

method (Figure 4).[32,33,100,101] The ligand-mediated method utilizes the capping ligands binding selectively on exposed facets of nanoparticles. The template-assisted method employs sacrificial nanoparticles, such as metal oxide, metal sulfide, and metal nanoparticles. In the synthesis, target precursors are deposited as a shell or induce ion exchange on the surface of the templates for the formation of facet-controlled metal sulfides and phosphides.

4.1. Ligand-Mediated Direct Synthesis

Direct synthesis of facet-controlled metal sulfide and phosphide nanoparticles exploits capping ligands to promote the growth in the specific direction of nanoparticles.[35,102–105] When these ligands selectively attach to certain facets, a sparsely capped facet of a nanoparticle can grow faster than other facets. Therefore, the proper use of specific capping ligands can control the shape of nanoparticles. For example, Robinson et al.[104] introduced 1,2-hexadecanediol (HDD) and oleylamine (OAm) as capping ligands to control the shape of Cu_2S nanocrystals during the growth. When weak capping of HDD was allowed, the dipole interactions between the nanocrystals promoted the attachment of nanoparticles along their chalcocite the *c*-axis facets, resulting in the formation of (110)-faceted nanorods. However, when HDD was replaced with strong capping OAm, the interactions between $Cu_{2-x}S$ nanocrystals were obstructed, and lateral ripening was promoted for the formation of (110) and (100)-faceted nanoplatelets (**Figure 8**a). Thermal decomposition of CuSCN in oleylamine also formed hexagonal nanoplates of $Cu_{1.94}S$ with $(\bar{1}00)$-faceted hexagonal face, indicating the effect of OAm on the $(\bar{1}00)$ facet stabilization.[106] Facet control induced by the variation of capping ligands is also seen in the results of An et al.[105] that 1-hexadecylamine (HDA) served as a capping ligand to expose the (001) and led to the formation of hexagonal CuS nanoplatelets. When $Al_2(SO_4)_3$ was utilized instead of HDA, both Al^{3+} and SO_4^{2-} were responsible for the growth of $Cu_{1.12}S$ nanocrystals into tetrahedra bound by (111) facets.

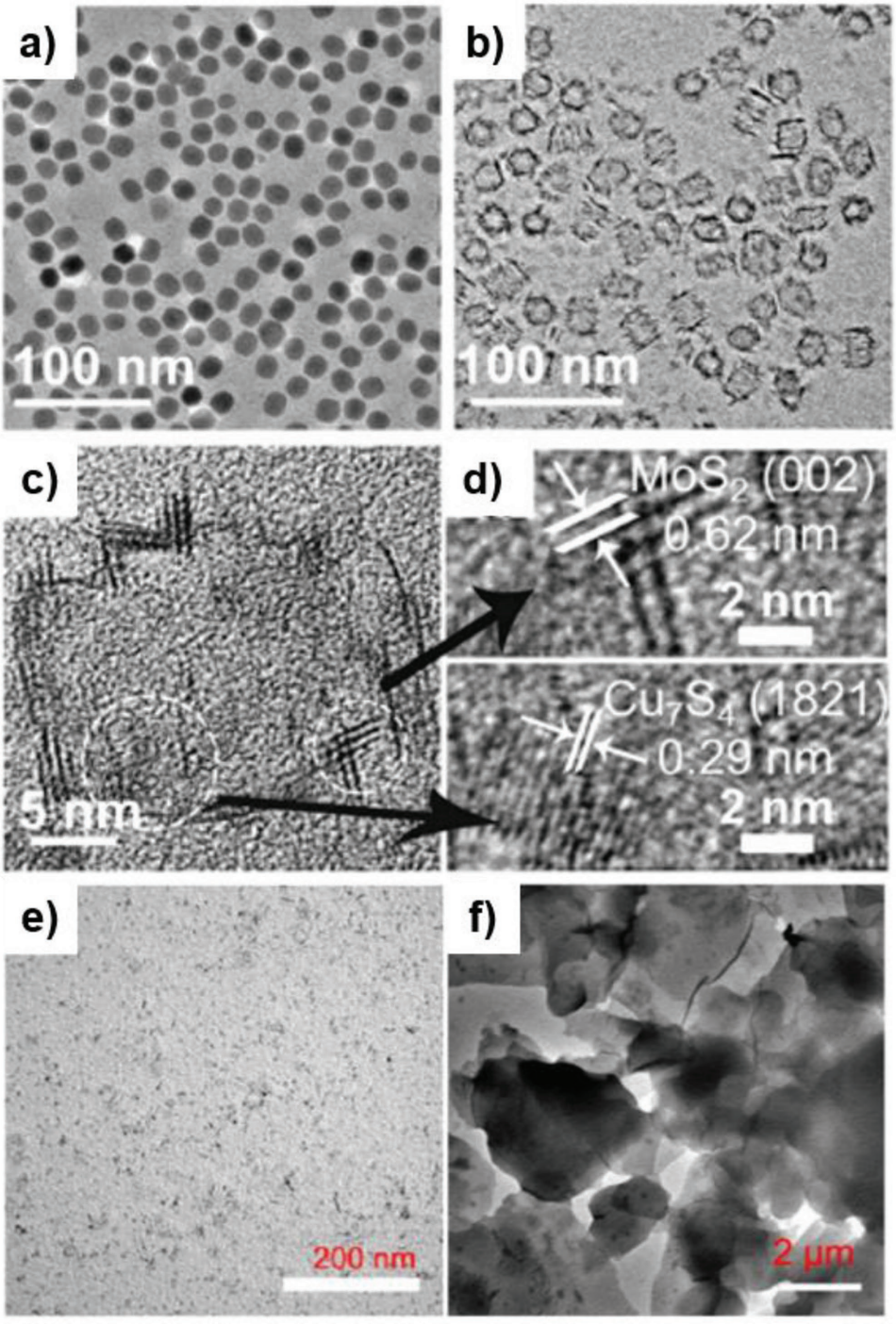

Figure 7. a,b) TEM images of Cu_7S_4 template (a) and hollow Cu_7S_4@MoS_2 (b). c,d) HRTEM images of hollow Cu_7S_4@MoS_2. e,f) TEM images of hollow Cu_7S_4@MoS_2 after chemical etching (e) and MoS_2 without Cu_7S_4 template (f). a–f) Reproduced with permission.[89] Copyright 2016, Wiley-VCH.

Facet-controlled metal phosphides also can be synthesized by utilizing a similar strategy. According to Popczun et al.,[107] the presence of trioctylphosphine oxide (TOPO) in a cosolvent of TOP and OAm enabled the generation of CoP nanostructures with their branches predominantly enclosed by (111) facets (Figure 8b). According to the description, the TOP is the primary phosphorus source, while TOPO is involved in shape control of (111) faceted nanorods. In another case, Ni_2P nanorods could be synthesized by using TOP as the capping ligand. Octyl groups generated by the decomposition of Ni–TOP complexes drove the morphological transformation of Ni_2P nanospheres into nanorods.[108] It was proved that the octyl groups selectively adhered to the (210) facets

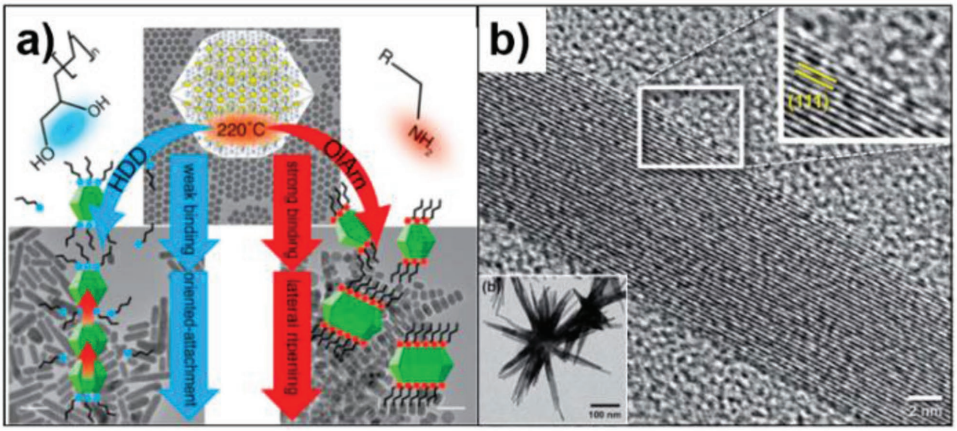

Figure 8. a) Effects of 1,2-hexadecanediol (left) and oleylamine (right) on Cu_2S nanoparticles as capping ligands. Scale bar: 50 nm. Reproduced with permission.[104] Copyright 2017, American Chemical Society. b) TEM and HRTEM images of a nanorod branch of a representative CoP nanostructure with exposed (111) facets. Reproduced with permission.[107] Copyright 2015, The Royal Society of Chemistry.

and blocked the growth on these facets whereas selective growth along [001] direction continued to yield Ni_2P nanorods.

4.2. Template-Assisted Indirect Synthesis

4.2.1. Ion Exchange Method

Ion exchange of well-defined nanoscale templates can allow the formation of facet-controlled metal sulfides and phosphide nanoparticles. Generally, ion exchange events on the surface of nanoparticles circumvent the growth of these nanoparticles along certain facets. In this manner, cation exchange has displayed its versatility in the development of facet-controlled metal sulfides and phosphides.[109–112] The high surface-to-volume ratio of nanoparticles and low activation barrier for cations to diffuse into them enable the usage of ambient experimental conditions. Metastable templates can facilitate cation exchange which leads to the formation of novel facet-controlled metal sulfides. Yuan et al.[111] utilized Cu_7S_4 nanocrystals as templates for the formation of γ-MnS nanocrystals via cation exchange, since the abundant Cu vacancies could encourage the cation exchange. Careful control of temperature and time produced compositionally altered nanocrystals whose area of γ-MnS varied. Although the intermediates from Cu_7S_4 to γ-MnS show dissimilar chemical compositions, all of them inherited the morphology of the Cu_7S_4 templates (**Figure 9**a–f). Cation exchange can also enable the synthesis of facet-controlled metal phosphides. According to De Trizio et al.,[112] hexagonal $Cu_{3-x}P$ nanoplatelets can serve as a template for the formation of wurtzite InP nanoplatelets. The Cu^+ ions in the corners are more highly active than top or bottom facets of a $Cu_{3-x}P$ nanoplatelet because of their low-coordination environment, so that the exchange of Cu^+ ions with In^{3+} ions occurred at the corners and to the lateral edges (Figure 9g–l).

Compared to the cation exchange condition, anion exchange method has been much rarer for the synthesis of facet-controlled metal sulfides and phosphides. The sluggish mobility of anions due to their generally larger radii than those of cations constrains the use of anion exchange method. In order to facilitate anion exchange, harsh conditions, detrimental to the morphology of a template, might be necessary.[87] The longer reaction time and higher temperature of anion exchange method can form amorphous phases in templates whose anion framework is severely perturbed. Hence, nanoparticles that have undergone anion exchange reaction in milder conditions to retain the shape of templates often result in core–shell structures. For instance, Wu et al.[113] partly converted Cu_2O into Cu_xS phases by the utilization of Na_2S as the anion source under ambient conditions and produced $Cu_2O@Cu_xS$ core–shell nanocrystals. In the case of the partial ion exchange or template mediated growth, the postetching of the core might result in the facet-controlled hollow morphology. Therefore, the subsequent etching of the Cu_2O core by HCl yielded regular hexahedral (RH) $Cu_{1.8}S$ nanocages and rhombohedral dodecahedral (RD) $Cu_{1.75}S$ nanocages from RH and RD Cu_2O templates. Interestingly, further cation exchange of these products with Cd^{2+} ions could form RH and RD CdS nanocages enclosed by six {100} and twelve {110} facets, respectively (Figure 9m).

4.2.2. Template-Mediated Growth Method

The template-mediated growth is a distinct strategy from ion exchange. The epitaxial overgrowth on the templates can result in facet-controlled metal sulfides and phosphides core–shell structure.[32,100,114] Compared to the ion exchange, the template-mediated growth needs a higher reaction temperature due to the high thermal decomposition temperature of additional precursors. Kim et al.[100] utilized Rh-doped PbS nanocubes as a template for the secondary growth of $Rh_3Pb_2S_2$ on its surfaces. The Rh, as a dopant, plays a critical role in formation of well-faceted PbS nanocube. During the secondary growth at high temperature, the additional growth of $Rh_3Pb_2S_2$ occurs on the Rh-doped PbS nanocubes to produce a facet-controlled PbS@$Rh_3Pb_2S_2$ core–shell structure. The {110} $Rh_3Pb_2S_2$ layers were grown on the {200} facets of PbS core. As mentioned before, the postetching of the core can result in the facet-controlled hollow nanoparticles. The metastable PbS is dissolved during the HNO_3 etching process to produce {110} faceted hollow $Rh_3Pb_2S_2$ nanocages (**Figure 10**a–d). In another case, $Cu_{2-x}S$

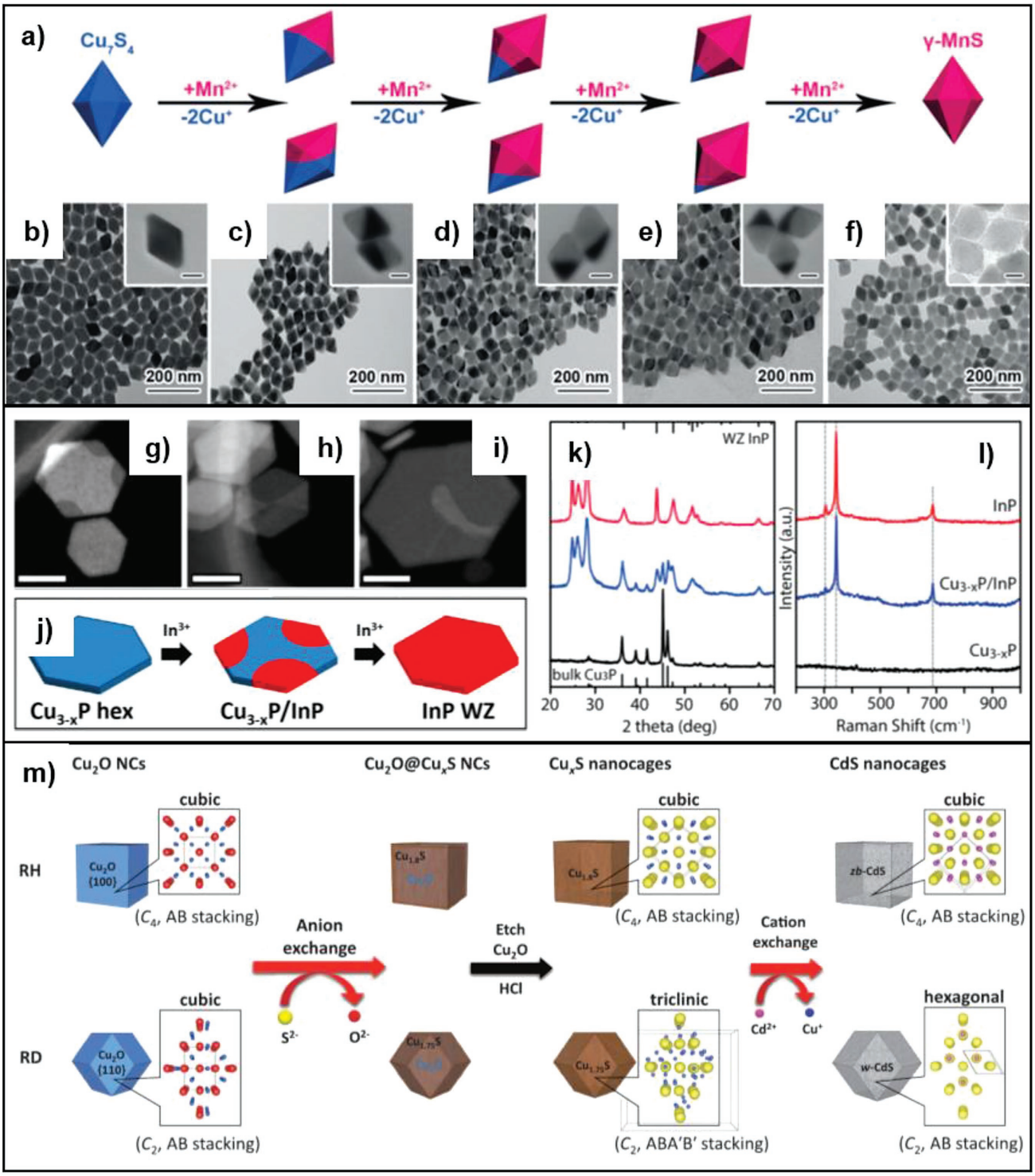

Figure 9. a–f) Schematic illustration of the cation exchange process and its corresponding TEM images: the initial Cu_7S_4 nanocrystals changes into γ-MnS gradually during cation exchange process. Reproduced with permission.[111] Copyright 2017, Wiley-VCH. g–l) HAADF-STEM, schematic illustration, XRD patterns and Raman spectra of $Cu_{3-x}P$/InP heterostructures at different cation exchange states. Reproduced with permission.[112] Copyright 2015, American Chemical Society. m) Schematic illustration for phase transitions of Cu_2O induced by the shape-dependent anionic frameworks in anion-exchange reactions and the subsequent cation-exchange reactions. Reproduced with permission.[113] Copyright 2016, The American Association for the Advancement of Science.

hexagonal platelets were used for template-mediated growth.[32] According to Yoon et al., facet-controlled hollow Rh_2S_3 nanoprisms were synthesized via facile one-pot synthesis method, followed by chemical etching. The different rates of formation between $Cu_{2-x}S$ and Rh_2S_3 enables the one-pot synthesis method for $Cu_{2-x}S@Rh_2S_3$ core–shell structure, which is

treated HCl to remove the metastable $Cu_{2-x}S$ templates and to selectively produce facet-controlled hollow Rh_2S_3 nanoprisms. The hollow orthorhombic Rh_2S_3 nanoprisms have $(1\bar{1}0)$ facets on hexagonal faces and (211) and $(21\bar{1})$ facets on six sides of the prisms (Figure 10e–g). It was recently shown that IrS_y phase can be epitaxially grown on the $Cu_{2-x}S$ nanoplates to form a copper sulfide plate surrounded by an IrS_y shell.[114]

5. Hollow and Facet-Controlled Metal Sulfides and Phosphides as Promising Water-Splitting Electrocatalysts

5.1. Electrocatalytic Performance of Hollow Metal Sulfides and Phosphides

While investigating the composition of a nanostructure to metal sulfides and phosphides that display reasonable performance in electrocatalytic water splitting, many studies have concentrated on increasing the number of the catalytically active sites to further enhance the performance. The utilization of hollow nanostructures has proven to be an effective method for accomplishing this goal.

According to Yu et al.,[29] the water-splitting performance of hollow CoP nanoparticles (CoP_h) deposited on N-doped graphene (NG) in 1.0 M KOH electrolyte solution was superior to that of the solid spherical CoP counterparts (CoP_s) (**Figure 11**). The overpotentials of CoP_h/NG to drive each HER and OER at a current density of 10 mA cm^{-2} were 83 and 262 mV, respectively, while those of CoP_s/NG were 109 and 289 mV, respectively. The lower overpotentials of CoP_h/NG than those of CoP_s/NG demonstrated that the hollow morphology of CoP_h encourages water-splitting electrocatalysis. Furthermore, the measurement of double-layer capacitance (C_{dl}) could evaluate the electrochemical active surface areas of CoP_h/NG and CoP_s/NG due to the positive proportional relationship between C_{dl} and ECSA. The C_{dl} (113 mF cm^{-2}) of CoP_h/NG was larger than that (99 mF cm^{-2}) of CoP_s/NG, indicating larger ECSAs. This could further imply that larger ECSAs of CoP_h contributed to higher electrocatalytic water-splitting performance. From the above example, it is noteworthy that the hollow morphology boosted both HER and OER performance without any change of chemical composition.

The majority of studies point out that the improved electrocatalytic HER and OER performance of metal sulfides and phosphides employing the hollow architecture is ascribed to the high density of active sites of reaction intermediates of the water-splitting coordinate, and a thin intrashell that allows short diffusion pathways.[115] The additionally exposed inner surface of a hollow nanostructure as well as its outer surface allows more contact of water molecule reactants. Moreover, the porosity or defects on the surface of a hollow nanostructure provide channels which connect its internal void and surrounding electrolyte, decreasing both ion diffusion distance and ion transport resistance. Such advantages upgrade the electrocatalytic water-splitting performance of metal sulfides and phosphides. However, the increase in the number of active sites by adopting a hollow nanostructure is not sufficient to make metal sulfides and phosphides compete with commercial water-splitting electrocatalysts comprised of noble metals. This can be attributed to the physical limit of the number of active sites in hollow nanostructures. Hence, a complementary strategy such as modulating the nature of active sites is necessary for pushing the boundary of catalytic performance in a grander scale.

5.2. Electrocatalytic Performance of Facet-Controlled Metal Sulfides and Phosphides

A great portion of research has focused on improving the intrinsic reactivity of active sites on the surface of nanostructures. For this, there have been efforts to synthesize facet-controlled metal sulfide and phosphide nanostructures bound by particular facets which exert high catalytic activity for water splitting.[33,116] These active facets generally expose low-coordinated metal atoms and sulfur/phosphorous rich environment. Kim et al.[100] reported the direct comparison between $Rh_3Pb_2S_2$ nanocages with defined and undefined facets for HER activity. In **Figure 12**, it is clear that the facet-controlled $Rh_3Pb_2S_2$ nanocages exhibit greatly enhanced HER activity compared to the counterpart. Computational calculation presented the theoretical evidence of facet-dependency in electrocatalytic activity in metal sulfides. According to Feng et al.,[33] Ni_3S_2 nanosheet arrays with high-index facet exposed displayed high electrocatalytic HER and OER performance (**Figure 13**). The HER and OER activities of mainly $\{\bar{2}10\}$-faceted Ni_3S_2 nanosheet array were higher than those of mostly {001}-faceted one in the electrochemical measurements. In addition, the HER and OER activities of nanosheet array enclosed by both $\{\bar{2}10\}$ and {001} facets were in between those predominantly possessing one of the two facets (Figure 13c). DFT calculations of the ΔG_H on $(\bar{2}10)$ and (001) facets corroborated the idea that $(\bar{2}10)$ facets are more active than (001) facets toward HER. Computation of the ΔG_H of the active sites on Ni_3S_2 nanosheet arrays shows that ΔG_H of Ni and S sites on the $(\bar{2}10)$ facet are 0.496 and 0.623 eV, respectively, and are closer to zero than those of the (001) facet (Figure 13f). The smaller ΔG_H on the $(\bar{2}10)$ facet could be attributed to both less crowdedness and lower-coordination Ni and S sites existing at terrace and step edges on the $(\bar{2}10)$ facet. Furthermore, the free energy diagram of the OER on the $(\bar{2}10)$ and (001) surfaces demonstrate the highly active OER on the $(\bar{2}10)$ surface compared to the (001) surface. When a bias applied (black line), the required overpotentials are 0.58 V for the $(\bar{2}10)$ surface and 0.70 V for (001) surface, which indicates the $(\bar{2}10)$ surface shows enhanced catalytic activity toward OER (Figure 13g).

Facet-controlled metal phosphides also showed their potential to serve as promising HER catalysts. Hansen et al. discovered that facet control of Ni_2P nanowires could present more available HER-active facets than the (0001) facet, which was reported as the most active facet for HER in many cases of nickel phosphide HER nanocatalysts.[35] They calculated the transition state energy (G^{TS}) for Tafel mechanism (H_{ads} + $H_{ads} \rightarrow H_2$) instead of the ΔG_H, since G^{TS} was the rate-limiting barrier to complete HER in their experimental scope. The $(\bar{1}\bar{1}20)$ and $(\bar{1}\bar{1}21)$ facets of Ni_2P nanowires were

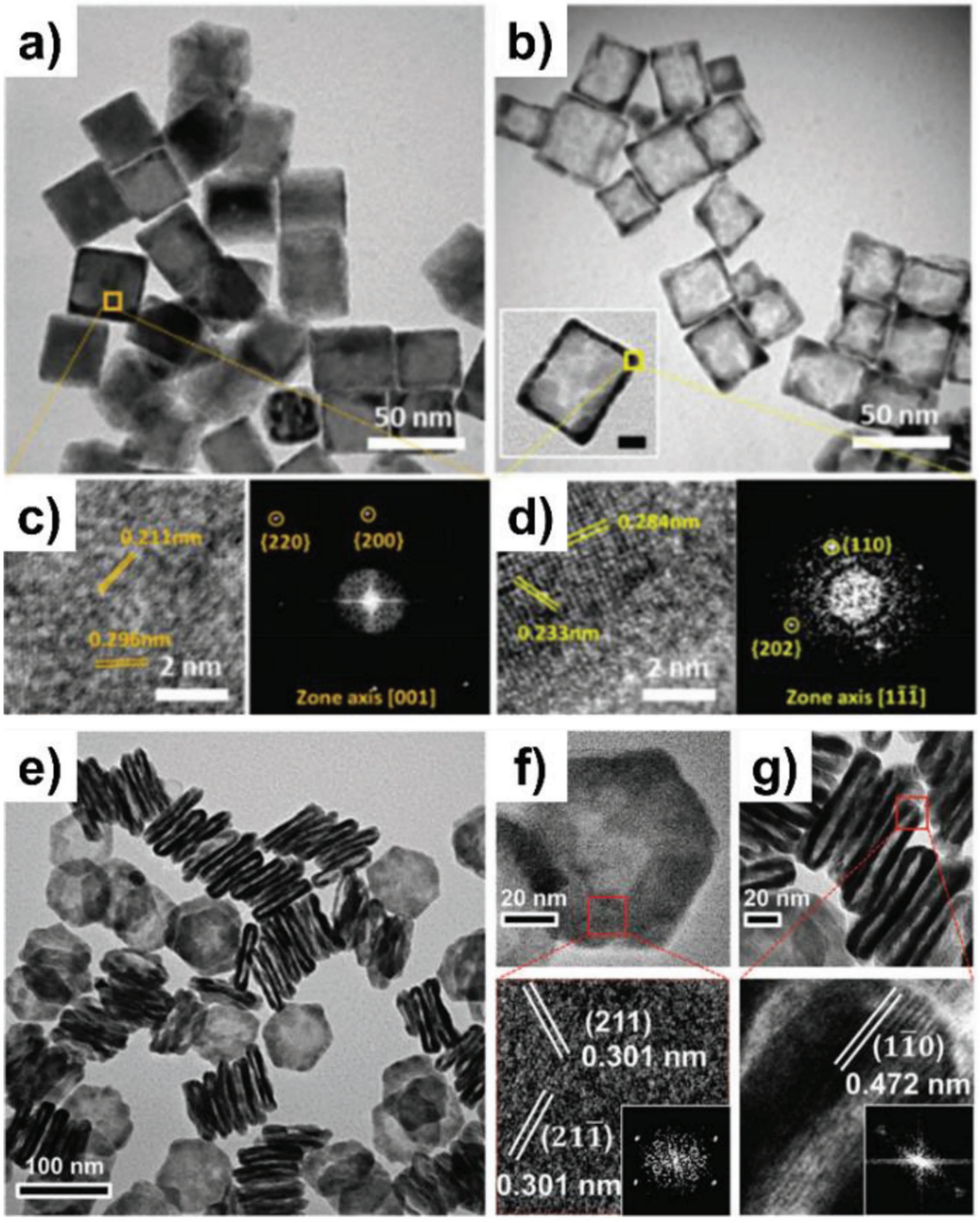

Figure 10. a–d) HRTEM images and corresponding FFT patterns of PbS@$Rh_3Pb_2S_2$ core–shell and hollow $Rh_3Pb_2S_2$ nanocages. a–d) Reproduced with permission.[100] Copyright 2018, The Royal Society of Chemistry. e–g) HRTEM images and corresponding FFT patterns of hollow facet-controlled Rh_2S_3 nanoprisms. e–g) Reproduced with permission.[32] Copyright 2016, The Royal Society of Chemistry.

more favorable to driving the Tafel mechanism than the (0001) facet because G^{TS} of $(\bar{1}\bar{1}20)$ and $(\bar{1}\bar{1}21)$ facets were lower than that of the (0001) facet, according to DFT calculations. This was ascribed to the facile and moderate bonding between hydrogen intermediates (H_{ads}) attached to phosphorous-stabilized Ni-Ni bridge sites of $(\bar{1}\bar{1}20)$ facets (**Figure 14**). Hu et al.[117] predicted by the DFT calculations and ab initio atomistic thermodynamics that the (111) facet of CoP surface would be more HER-active than (100), (110), and (011) facets. The comparison among those facets in terms of the ΔG_H indicated that (011), (110) and (111) facets would exert reasonable HER activities. On top of that, the stability test of the hydrogen-covered facets under 300 K and 1 atm H_2 revealed that the trend was (111) > (100) ≈ (110) >> (011). On account of

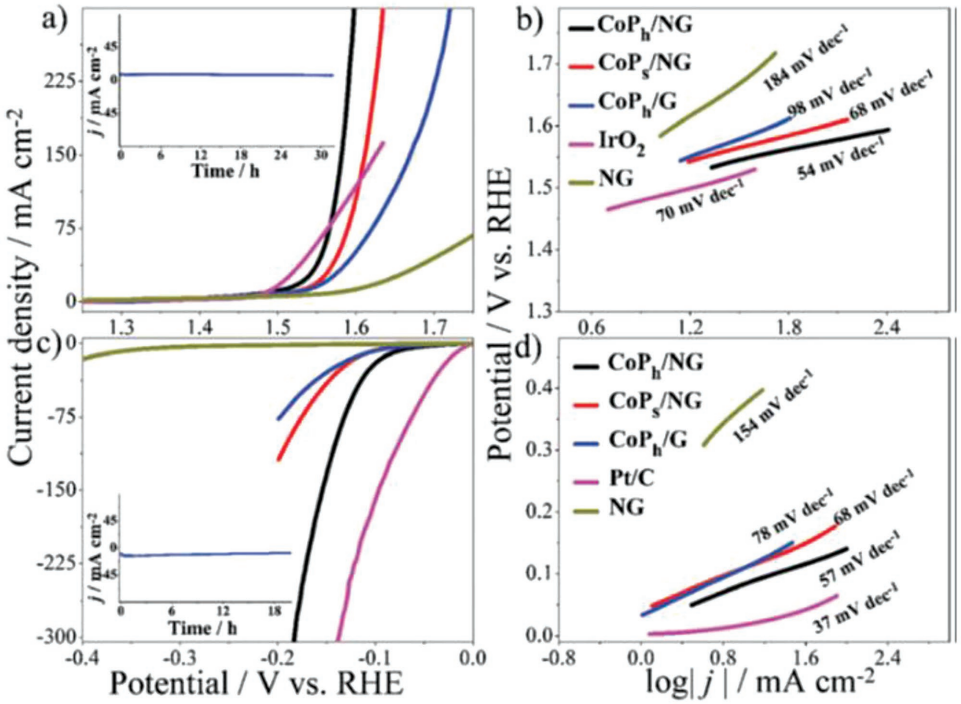

Figure 11. a–d) The polarization curves and Tafel plots of CoP_h/NG, CoP_s/NG, CoP_h/G, NG, commercial IrO_2, and Pt/C for OER (a,b) and HER (c,d) in 1.0 M KOH with a scan rate of 5 mV s^{-1}. a–d) Reproduced with permission.[29] Copyright 2016, The Royal Society of Chemistry.

closer-to-zero ΔG_H and high stability, CoP (111) facets would display both high and long-term HER activity. This phenomenon could be further explained by the cooperative effect of Co–Co bridge sites and P top sites residing on the (111) facet. Interestingly, according to the above result, intentional facet control of a CoP nanostructure to expose the (111) facet could yield highly active HER catalyst based on CoP.[103] After confirming more active facets for HER, the facet-controlled metal sulfide and phosphide nanostructures would help researchers acquire unprecedented high-performing HER catalysts.

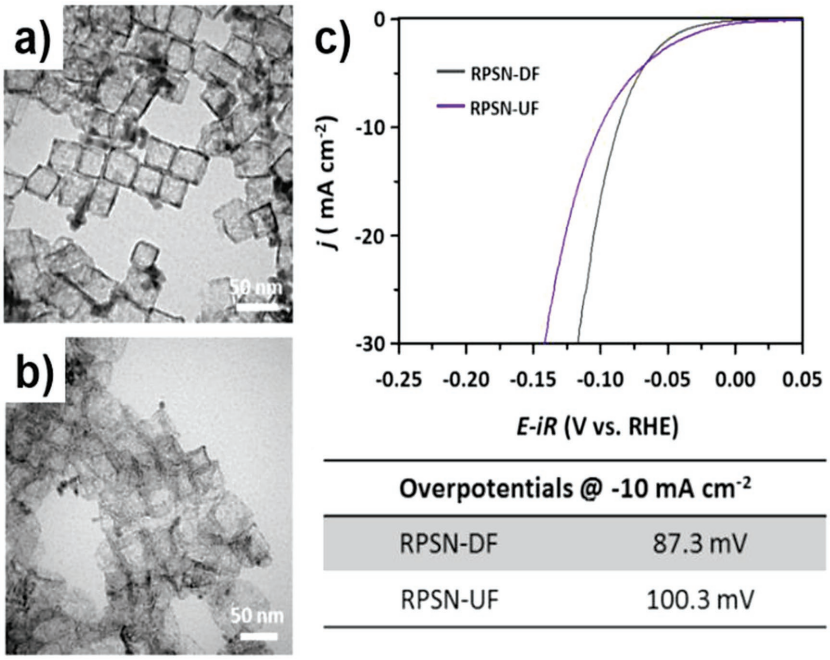

Overpotentials @ -10 mA cm^{-2}	
RPSN-DF	87.3 mV
RPSN-UF	100.3 mV

Figure 12. a,b) HRTEM image of $Rh_3Pb_2S_2$ nanocages with facet defined and undefined. c) The polarization curves of $Rh_3Pb_2S_2$ nanocages with facet defined and undefined and overpotentials at −10 mA cm^{-2}. a–c) Reproduced with permission.[100] Copyright 2018, The Royal Society of Chemistry.

The intermediates of OER include a variety of chemical species, and they change into other chemical moieties after interacting with the catalytic active sites of catalysts, which greatly complicates the mechanism of OER. Therefore, contrary to the obvious effect of nanocatalyst facets on HER performance, establishing such correlation between facets and OER activity via DFT calculations of the adsorption energy of OER intermediates is very difficult.[118] However, the possibility of increasing the reactivity of OER catalysts by facet control has been empirically demonstrated in the case of metal oxides. As reported by Chen et al.,[34] the electrocatalytic OER activity of nanooctahedra of Co_3O_4 enclosed by (111) facets surpassed that of nanocubes of Co_3O_4 bound by (100) facets due to higher density of catalytically active Co^{3+} ions on (111) facets than (100) ones (**Figure 15**a,b). Furthermore, Kakizaki et al.[119] demonstrated that the OER activity of β-MnO_2 bipyramid

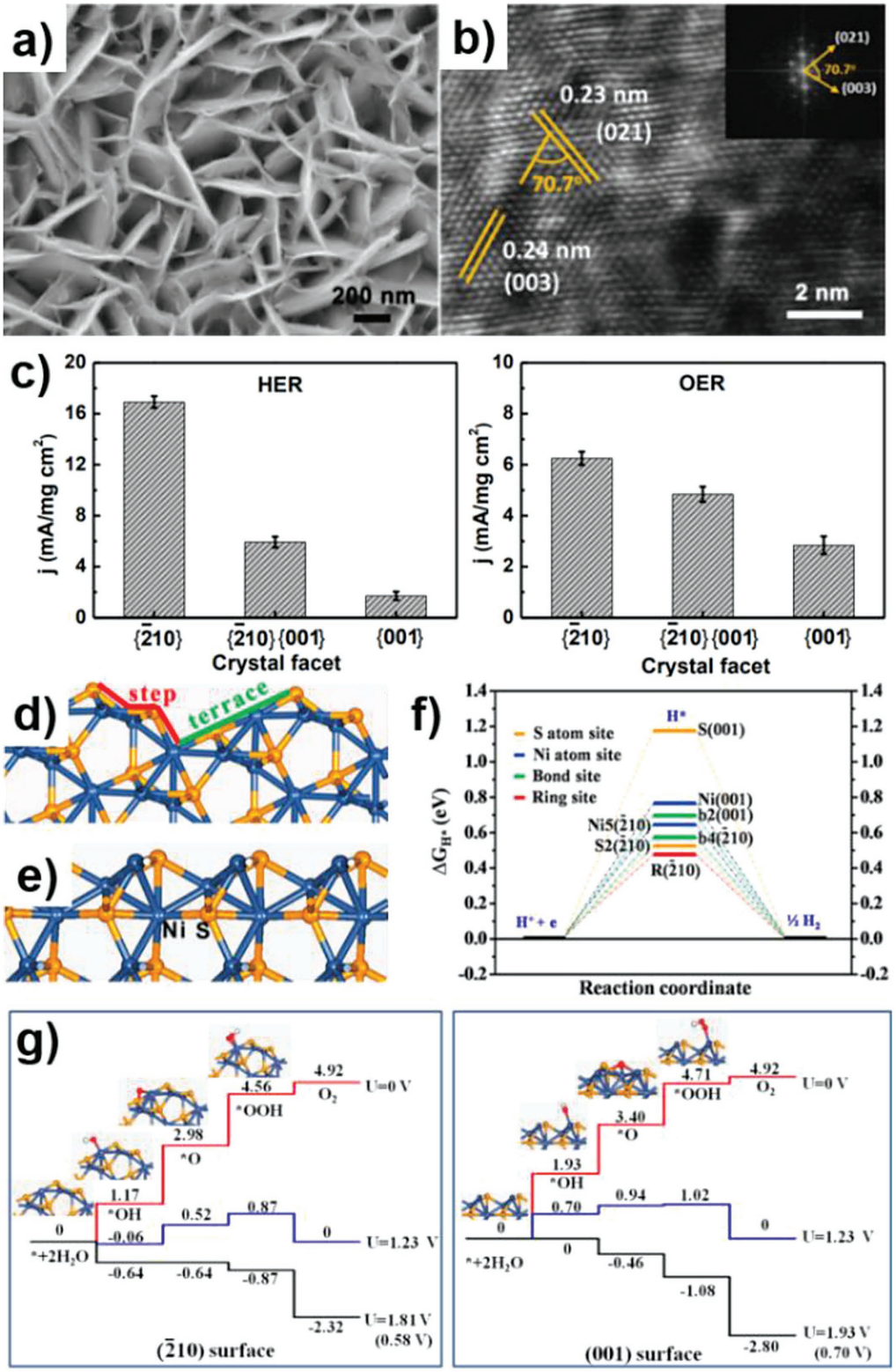

Figure 13. a,b) SEM and HRTEM images of {$\bar{2}$10}-faceted Ni_3S_2 nanosheets. c) Comparison of the catalytic activity for HER and OER at the overpotential of 260 mV in neutral media for Ni_3S_2 nanosheets with different exposed facets. d,e) Most stable surface models of ($\bar{2}$10) (d) and (001) (e) surfaces of Ni_3S_2. f) Calculated ΔG_H over ($\bar{2}$10) and (001) surfaces at equilibrium potential. g) Free energy diagram for the each step of the OER on the ($\bar{2}$10) and (001) surface of Ni_3S_2 nanosheet at the different applied potentials. a–g) Reproduced with permission.[33] Copyright 2015, American Chemical Society.

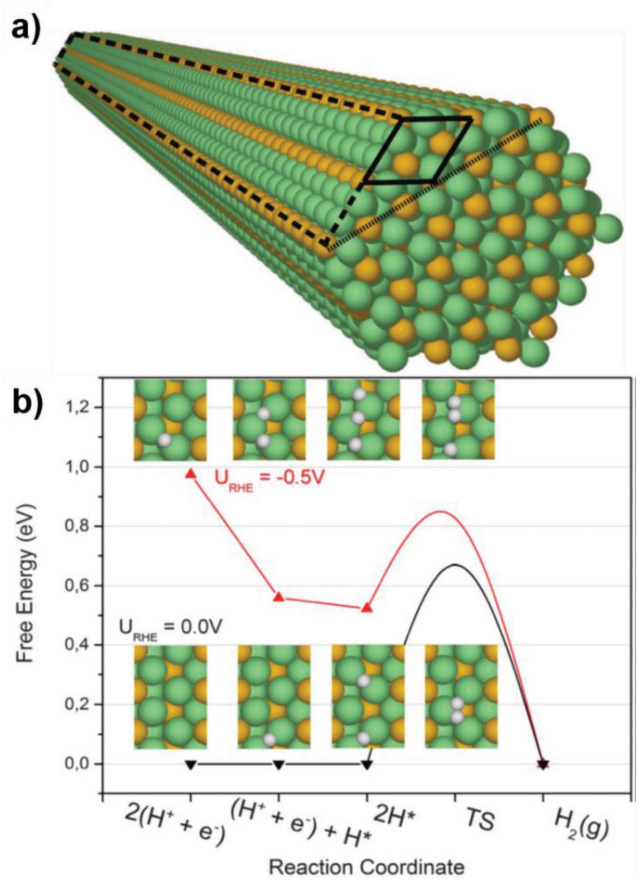

Figure 14. a) Model of a Ni_2P nanowire crystal. The solid lines show (0001) plane of the unit cell, coarsely dashed lines show a $(10\bar{1}0)$ plane, and the finely dashed line shows the $\pm(11\bar{2}0)$ plane. b) Free energy diagram of the Volmer–Tafel reaction on the $(10\bar{1}0)$ facet and the configuration of each point. Each color indicates Ni (green), P (yellow), and H (white). a,b) Reproduced with permission.[35] Copyright 2015, The Royal Society of Chemistry.

samples with (101) facets outperformed that of nanowire samples with (110) facets, since higher density of Mn^{3+} ions on (101) facets stabilized Mn^{3+} intermediates better than (111) ones with lower Mn^{3+} density during OER (Figure 15c–e). As with the metal oxide examples, facet control of metal sulfides and phosphides might also contribute to the enhancement of the OER activity as well as the HER counterpart.

5.3. Tendency of Electrocatalytic Performance in Hollow and/or Facet-Controlled Metal Sulfides and Phosphides

Considering all the above reported examples, metal sulfides and phosphides with hollow or facet-controlled nanostructures have shown promising prospects for raising their electrocatalytic water-splitting performance. On top of that, the overall trend of the varying overpotentials to drive a current density of 10 mA cm^{-2} during HER and OER electrocatalysis in acidic and alkaline electrolyte supports the positive outlook of endowing nanostructures with morphological factors that are hollowness and facets (**Figure 16**). According to the various reports, HER is usually sluggish in alkaline electrolyte compared with that in acidic electrolyte.[21,92,102,120] For example, Yan et al.[120] reported the hollow FeP nanotubes for HER electrocatalysts that showed 88 mV of overpotential in acidic electrolytes and 120 mV of overpotential in alkaline electrolytes. In addition, the facet controlled Ni_5P_4 showed remarkable HER activity in acidic electrolyte with overpotential of 35.4 mV. In contrast, in alkaline electrolyte, the overpotential of Ni_5P_4 for HER was increased by 11.7 mV.

The electrolyte effect in HER is relatively small compared to the effect in OER, due to the faster reaction kinetics of HER. Therefore, the metal sulfides and phosphides could be employed in wide range of pH, but most of the metal sulfide- and phosphide-based OER electrocatalysts have been developed for use in alkaline electrolyte; there exists a large difference in reaction kinetics of between alkaline OER and acidic OER.[26] For example, Hu et al.[121] reported the performance of $Ni_{40}Fe_{40}P_{20}$ electrocatalysts for both alkaline OER and acidic OER. The overpotential of $Ni_{40}Fe_{40}P_{20}$ to drive alkaline OER at a current density of 10 mA cm^{-2} was 219 mV while that of $Ni_{40}Fe_{40}P_{20}$ to reach the same current density for acidic OER was 540 mV.

Figure 16 and **Tables 2** and **3** that display the overpotentials and Tafel slopes of spherical and hollow nanoparticles reveal that the catalytic reactions, in general, occur more favorably on the hollow nanostructures than the solid counterparts with or without considering chemical compositions. For example, hollow CoP nanoparticles required lower overpotential than spherical counterparts in both HER and OER, thus serving as better water-splitting electrocatalysts.[27,86] The overpotential of solid spherical iron phosphide nanoparticles in acidic HER was much higher than that of hollow ones. Hollow nanoparticles composed of diverse materials such as nickel cobalt sulfide, iron phosphide, and nickel cobalt phosphide were electrochemically more conducive to driving the same extent of current density than sphere nanoparticles, as judged by the lower alkaline OER overpotential of these hollow materials than spherical ones. Furthermore, the bar graphs in Figure 16a add weight to the expectation that facet-controlled nanoparticles have catalytic performance advantage over spherical nanoparticles. The HER overpotentials of facet-controlled nickel phosphides are much lower than spherical ones when the influence of their stoichiometry is considered. In addition, the electrocatalytic OER performance of spherical nickel sulfide and nickel iron phosphide nanoparticles is inferior to those of facet-controlled counterparts (Figure 16b).

Tables 2 and 3 exhibit Tafel slopes of nonhollow, hollow, and facet-controlled nanoparticles in both HER and OER. The Tafel slopes of nonhollow nanoparticles are larger than those of hollow and facet-controlled nanoparticles in both HER and OER. The large HER Tafel slopes of nonhollow nanoparticles reveal that the Volmer reaction is the RDS during the HER. In contrast, hollow and facet-controlled nanoparticles with HER Tafel slopes of less than 60 mV $decade^{-1}$ denote the Tafel and Heyrovsky reactions as the RDS (Table 2).[53] In Table 3, the OER Tafel slopes show similar tendency with that of the HER. According to section 2.1, the RDS of nonhollow nanoparticles during the OER is the adsorption of reactants to catalyst ($M + H_2O \rightarrow M–OH + H^+ + e^-$), while the RDS of hollow and facet-controlled nanoparticles is further oxidation reaction

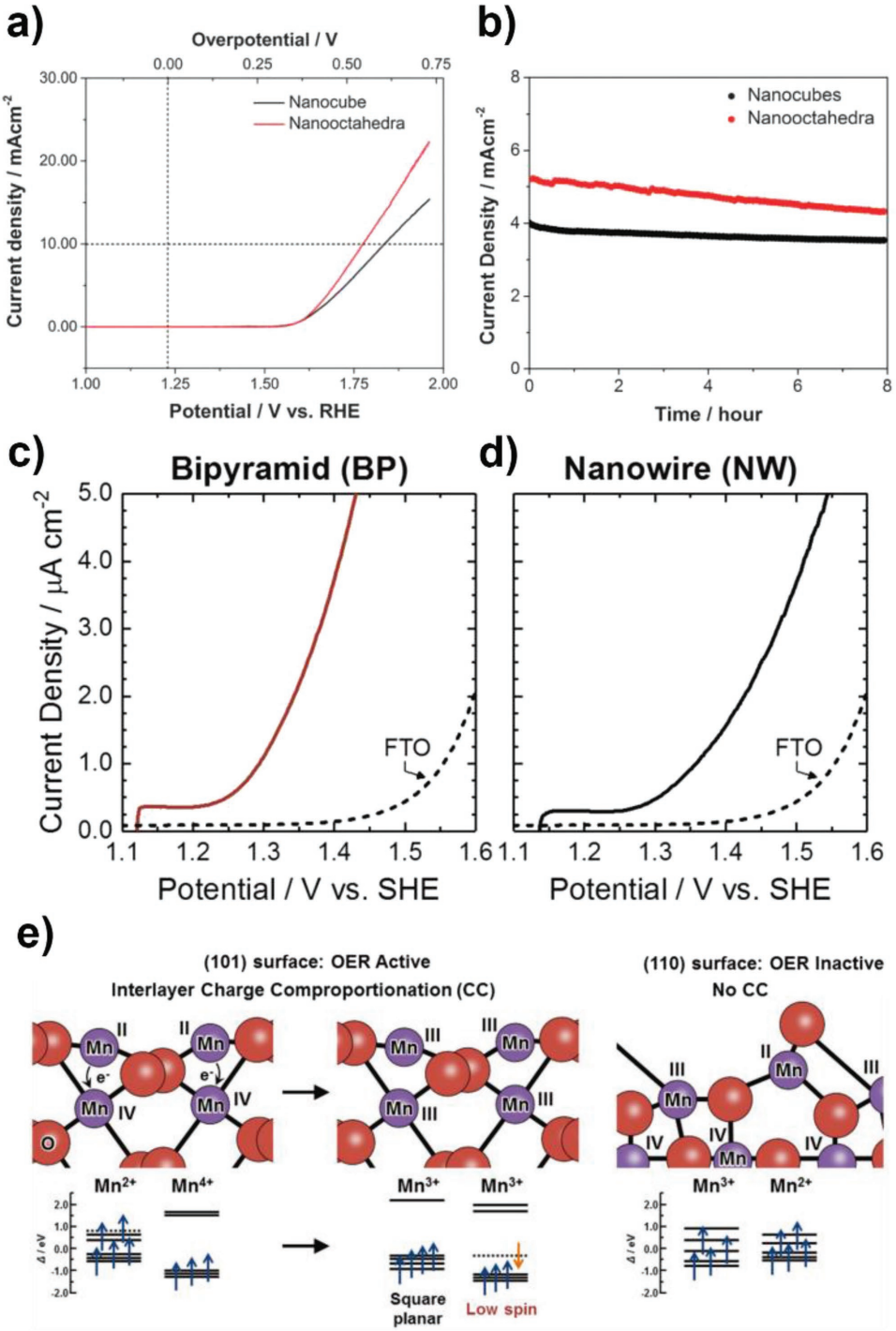

Figure 15. a,b) The polarization curves and stability test of Co_3O_4 nanocubes and nanooctahedra. a,b) Reproduced with permission.[34] Copyright 2015, The Royal Society of Chemistry. c,d) The polarization curves of MnO_2 bipyramid and nanowire. e) Schematic of facet dependence in OER activity. c–e) Reproduced with permission.[120] Copyright 2018, Wiley-VCH.

of intermediate (M–OH → M–O + H^+ + e^-). The aforementioned morphology-dependent Tafel slopes of hollow and/or facet-controlled structures are due to the fast reaction kinetics stemming from large surface area and/or highly active exposed facet.

6. Conclusions and Outlook

Two strategies to enhance the electrocatalytic water-splitting performance of metal sulfides and phosphides are increases in 1) the number of active sites and 2) the intrinsic activity of

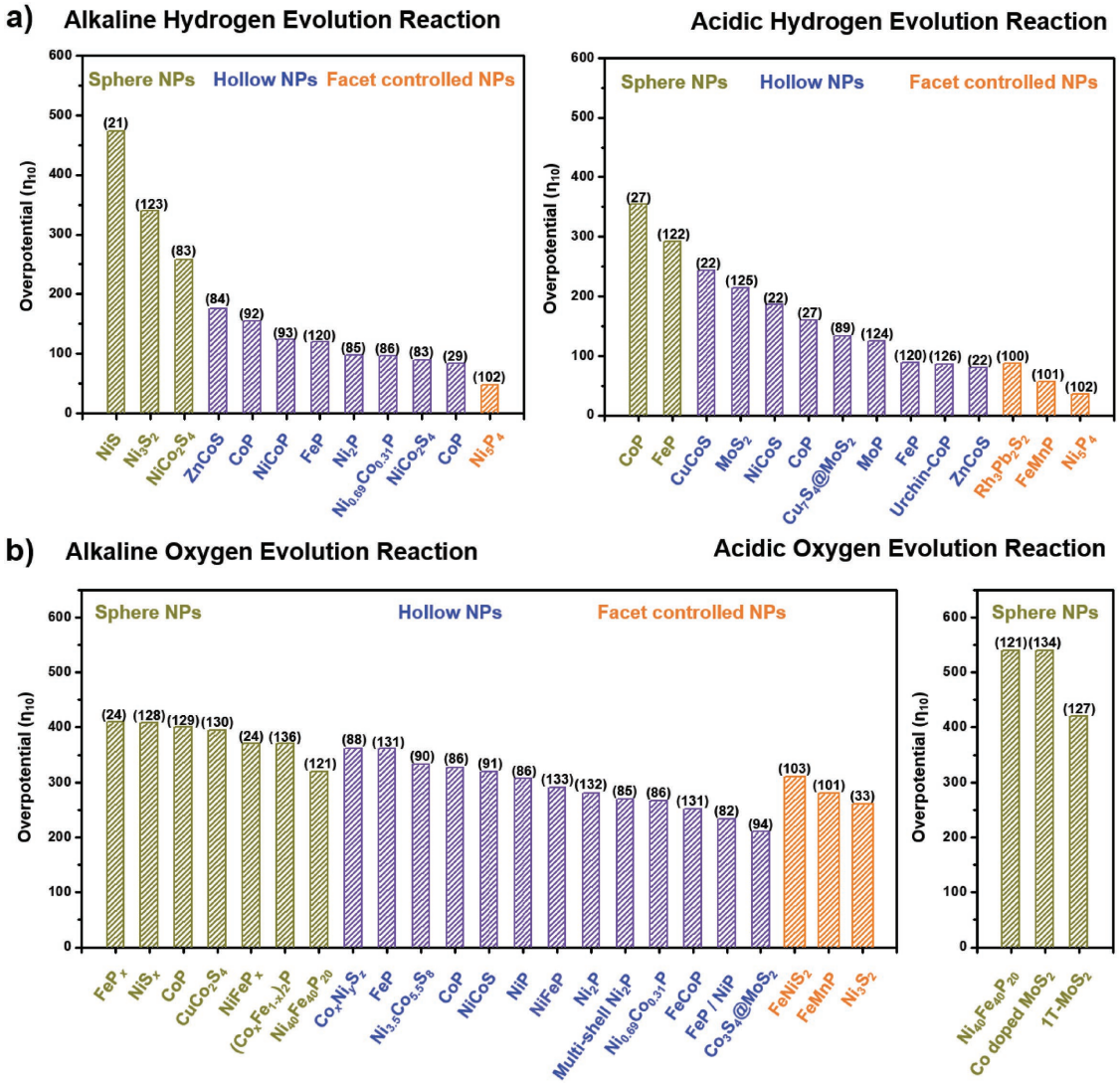

Figure 16. a,b) Comparison of HER (a) and OER (b) overpotential (@10 mA cm^{-2}) of metal sulfide and phosphides in both alkaline and acidic media. The numbers in parentheses refer to reference numbers.

active sites. Research on the development of facet-controlled and hollow metal sulfide and phosphide nanostructures has great importance because these materials can simultaneously increase the number of active sites and the intrinsic activity by their morphological characteristics. Hollow metal sulfide and phosphide nanostructures possess larger density of active sites than solid ones, contributing to the improvement in both HER and OER electrocatalysis. Furthermore, morphology and facet-controlled nanostructures, usually bearing low-coordinated number of metals and abundant sulfur/phosphorous atoms, demonstrate their capacity to become more excellent water splitting catalysts than nanostructures without distinctive shapes. In general, the Gibbs free energy for hydrogen adsorption (ΔG_H) on the facets of nanostructures calculated to be closer to zero via DFT calculations reinforces the superiority of facet control. Unfortunately, the lack of profound studies on the complicated mechanism of OER electrocatalysis impedes the clarification of the specific catalytic species directing OER. Therefore, there is difficulty in the direct application of the ΔG_H of OER intermediates to find the most OER-active facet of nanostructures. It is essential to conduct more studies investigating the actual catalytic species that participate in OER electrocatalysis in order to establish a firm standard to judge which facet is the most active toward electrocatalytic OER. Despite little accumulated data of electrochemical measurements which compare the electrocatalytic water-splitting performance of facet-controlled nanostructures with the performance of nanostructures without definitive facets, a reasonable number of DFT calculations add weight to the idea that deliberately shaping a nanostructure predominantly bound by particular facets can be effective in obtaining highly active water-splitting electrocatalysts.

Moving forward, we can conceive that grafting facets onto hollow nanostructures could improve the electrocatalytic water-splitting performance through their synergy. The rather harsh reaction conditions required for the Kirkendall effect are not beneficial to the formation of facet-controlled hollow nanoparticles.

Table 2. HER performance of metal sulfides and phosphides.

Catalyst	Structure	Overpotential	Tafel slope	Electrolyte	Ref.
		at 10 mA cm^{-2}	mV $decade^{-1}$		
NiS	Non-hollow	474	124	1 M KOH	[21]
$NiCo_2S_4$	Non-hollow	258	101	1 M KOH	[83]
FeP	Non-hollow	292	86	0.5 M H_2SO_4	[122]
CoP	Non-hollow	355	77	0.5 M H_2SO_4	[27]
	Hollow	159	59		
CoP/N-doped graphene	Non-hollow	109	68	1 M KOH	[29]
	Hollow	83	57		
MoS_2	Hollow	214	74	0.5 M H_2SO_4	[125]
FeP	Hollow	120	59.5	1 M KOH	[120]
MoP	Hollow	125	54	0.5 M H_2SO_4	[124]
$CoMoS_3$	Facet-controlled	171	56.9	0.5 M H_2SO_4	[135]
$Rh_3Pb_2S_2$	Facet-controlled	87.3	45.6	0.5 M H_2SO_4	[100]
FeMnP	Facet-controlled	57	54	0.5 M H_2SO_4	[101]
Ni_5P_4	Facet-controlled	35.4	48	0.5 M H_2SO_4	[102]
		47.1	56	1 M KOH	

Table 3. OER performance of metal sulfides and phosphides.

Catalyst	Structure	Overpotential	Tafel slope	Electrolyte	Ref.
		at 10 mA cm^{-2}	mV $decade^{-1}$		
Co_3S_4	Non-hollow	430	102	0.1 M KOH	[136]
CoP	Non-hollow	400	80	1 M NaOH	[129]
CoS_2	Non-hollow	400	96	0.1 M KOH	[137]
$CuCo_2S_4$	Non-hollow	395	115	0.1 M KOH	[130]
FeP	Hollow	361	58	1 M KOH	
CoP	Hollow	320	40	1 M KOH	[131]
FeCoP	Hollow	252	33	1 M KOH	
$Ni_{3.5}Co_{5.5}S_8$	Hollow	333	48.8	1 M KOH	[90]
Ni_2P	Hollow	270	40.4	1 M KOH	[85]
$FeNiS_2$	Facet-controlled	310	46	0.1 M KOH	[103]
FeMnP/GNF	Facet-controlled	280	57	0.1 M KOH	[101]

This makes the partial cation or anion exchange reaction involving shape-controlled templates the sole viable synthetic route to facet-controlled hollow nanoparticles. Leveraging this technique of postsynthetic etching of core–shell nanostructures, it was possible to acquire facet-controlled hollow nanostructures. A presynthetic computational prediction for the most highly active facet of a given chemical composition may also enable the customization of the optimally performing catalyst for water electrolysis.

Acknowledgements

J.J., T.K., and J.L. contributed equally to this work. This research was supported by the National Research Foundation of Korea with Grant Nos. 2017R1A2B3005682 and 2018R1C1B6004272, and the Korea Basic Science Institute under the R&D program (Project No. C38530) supervised by the Ministry of Science. The authors also thank to Korea UniversityFuture Research Grant for financial support.

Conflict of Interest

The authors declare no conflict of interest.

Keywords

electrolysis, facet-controlled, hollow structures, metal phosphides, metal sulfides

Received: October 15, 2018
Revised: December 1, 2018
Published online: February 1, 2019

[1] T. P. Hughes, J. T. Kerry, M. Álvarez-Noriega, J. G. Álvarez-Romero, K. D. Anderson, A. H. Baird, R. C. Babcock, M. Beger, D. R. Bellwood, R. Berkelmans, T. C. Bridge, I. R. Butler, M. Byrne, N. E. Cantin, S. Comeau, S. R. Connolly, G. S. Cumming, S. J. Dalton, G. Diaz-Pulido, C. M. Eakin, W. F. Figueira, J. P. Gilmour, H. B. Harrison, S. F. Heron, A. S. Hoey, J.-P. A. Hobbs, M. O. Hoogenboom, E. V. Kennedy, C.-Y. Kuo, J. M. Lough, R. J. Lowe, G. Liu, M. T. McCulloch, H. A. Malcolm, M. J. McWilliam, J. M. Pandolfi, R. J. Pears, M. S. Pratchett, V. Schoepf, T. Simpson, W. J. Skirving, B. Sommer, G. Torda, D. R. Wachenfeld, B. L. Willis, S. K. Wilson, *Nature* **2017**, *543*, 373.
[2] A. AghaKouchak, L. Cheng, O. Mazdiyasni, A. Farahmand, *Geophys. Res. Lett.* **2014**, *41*, 8847.
[3] R. Shortall, B. Davidsdottir, G. Axelsson, *Renewable Sustainable Energy Rev.* **2015**, *44*, 391.
[4] D. E. H. J. Gernaat, P. W. Bogaart, D. P. V. Vuuren, H. Biemans, R. Niessink, *Nat. Energy* **2017**, *2*, 821.
[5] D. Woolf, J. Lehmann, D. R. Lee, *Nat. Commun.* **2016**, *7*.
[6] N. S. Lewis, *Science* **2016**, *351*, aad1920.
[7] G. M. Joselin Herbert, S. Iniyan, E. Sreevalsan, S. Rajapandian, *Renewable Sustainable Energy Rev.* **2007**, *11*, 1117.
[8] Z. W. Seh, J. Kibsgaard, C. F. Dickens, I. Chorkendorff, J. K. Nørskov, T. F. Jaramillo, *Science* **2017**, *355*, eaad4998.
[9] C. G. Morales-Guio, L.-A. Stern, X. Hu, *Chem. Soc. Rev.* **2014**, *43*, 6555.
[10] Y. Xu, M. Kraft, R. Xu, *Chem. Soc. Rev.* **2016**, *45*, 3039.
[11] T. F. Jaramillo, K. P. Jørgensen, J. Bonde, J. H. Nielsen, S. Horch, I. Chorkendorff, *Science* **2007**, *317*, 100.
[12] L. C. Seitz, C. F. Dickens, K. Nishio, Y. Hikita, J. Montoya, A. Doyle, C. Kirk, A. Vojvodic, H. Y. Hwang, J. K. Norskov, T. F. Jaramillo, *Science* **2016**, *353*, 1011.
[13] J. A. Turner, *Science* **2004**, *305*, 972.
[14] X. Li, X. Hao, A. Abudula, G. Guan, *J. Mater. Chem. A* **2016**, *4*, 11973.
[15] T. Wu, M. L. Stone, M. J. Shearer, M. J. Stolt, I. A. Guzei, R. J. Hamers, R. Lu, K. Deng, S. Jin, J. R. Schmidt, *ACS Catal.* **2018**, *8*, 1143.
[16] Y. Yan, B. Y. Xia, B. Zhao, X. Wang, *J. Mater. Chem. A* **2016**, *4*, 17587.
[17] F. Wang, T. A. Shifa, X. Zhan, Y. Huang, K. Liu, Z. Cheng, C. Jiang, J. He, *Nanoscale* **2015**, *7*, 19764.
[18] M. A. Lukowski, A. S. Daniel, F. Meng, A. Forticaux, L. Li, S. Jin, *J. Am. Chem. Soc.* **2013**, *135*, 10274.
[19] P. Xiao, W. Chen, X. Wang, *Adv. Energy Mater.* **2015**, *5*, 1500985.
[20] X. Y. Yu, X. W. Lou, *Adv. Energy Mater.* **2018**, *8*, 1701592.
[21] N. Jiang, Q. Tang, M. Sheng, B. You, D.-E. Jiang, Y. Sun, *Catal. Sci. Technol.* **2016**, *6*, 1077.
[22] Z.-F. Huang, J. Song, K. Li, M. Tahir, Y.-T. Wang, L. Pan, L. Wang, X. Zhang, J.-J. Zou, *J. Am. Chem. Soc.* **2016**, *138*, 1359.
[23] D.-Y. Wang, M. Gong, H.-L. Chou, C.-J. Pan, H.-A. Chen, Y. Wu, M.-C. Lin, M. Guan, J. Yang, C.-W. Chen, Y.-L. Wang, B.-J. Hwang, C.-C. Chen, H. Dai, *J. Am. Chem. Soc.* **2015**, *137*, 1587.
[24] P. Li, H. C. Zeng, *Chem. Commun.* **2017**, *53*, 6025.
[25] X. Zou, Y. Zhang, *Chem. Soc. Rev.* **2015**, *44*, 5148.
[26] S. Anantharaj, S. R. Ede, K. Sakthikumar, K. Karthick, S. Mishra, S. Kundu, *ACS Catal.* **2016**, *6*, 8069.
[27] M. Liu, J. Li, *ACS Appl. Mater. Interfaces* **2016**, *8*, 2158.
[28] Y. Pan, K. Sun, S. Liu, X. Cao, K. Wu, W.-C. Cheong, Z. Chen, Y. Wang, Y. Li, Y. Liu, D. Wang, Q. Peng, C. Chen, Y. Li, *J. Am. Chem. Soc.* **2018**, *140*, 2610.
[29] X. Yu, S. Zhang, C. Li, C. Zhu, Y. Chen, P. Gao, L. Qi, X. Zhang, *Nanoscale* **2016**, *8*, 10902.
[30] C. Wei, Q. Lu, J. Sun, F. Gao, *Nanoscale* **2013**, *5*, 12224.
[31] E. J. Popczun, C. G. Read, C. W. Roske, N. S. Lewis, R. E. Schaak, *Angew. Chem., Int. Ed.* **2014**, *53*, 5427.
[32] D. Yoon, B. Seo, J. Lee, K. S. Nam, B. Kim, S. Park, H. Baik, S. Hoon Joo, K. Lee, *Energy Environ. Sci.* **2016**, *9*, 850.
[33] L.-L. Feng, G. Yu, Y. Wu, G.-D. Li, H. Li, Y. Sun, T. Asefa, W. Chen, X. Zou, *J. Am. Chem. Soc.* **2015**, *137*, 14023.
[34] Z. Chen, C. X. Kronawitter, B. E. Koel, *Phys. Chem. Chem. Phys.* **2015**, *17*, 29387.
[35] M. H. Hansen, L.-A. Stern, L. Feng, J. Rossmeisl, X. Hu, *Phys. Chem. Chem. Phys.* **2015**, *17*, 10823.
[36] H. Duan, D. Li, Y. Tang, Y. He, S. Ji, R. Wang, H. Lv, P. P. Lopes, A. P. Paulikas, H. Li, S. X. Mao, C. Wang, N. M. Markovic, J. Li, V. R. Stamenkovic, Y. Li, *J. Am. Chem. Soc.* **2017**, *139*, 5494.
[37] K. Wang, B. Huang, F. Lin, F. Lv, M. Luo, P. Zhou, Q. Liu, W. Zhang, C. Yang, Y. Tang, Y. Yang, W. Wang, H. Wang, S. Guo, *Adv. Energy Mater.* **2018**, *8*, 1801891.
[38] Y. Li, N. Li, X. Yan, X. Li, R. Wang, X. Zhang, *J. Mater. Sci.* **2017**, *52*, 11402.
[39] J. Masud, T. V. Nguyen, N. Singh, E. McFarland, M. Ikenberry, K. Hohn, C. J. Pan, B. J. Hwang, *J. Electrochem. Soc.* **2015**, *162*, F455.
[40] Z. Pu, I. S. Amiinu, Z. Kou, W. Li, S. Mu, *Angew. Chem., Int. Ed.* **2017**, *56*, 11559.
[41] Q. Qin, H. Jang, L. Chen, G. Nam, X. Liu, J. Cho, *Adv. Energy Mater.* **2018**, *8*, 1801478.
[42] I. C. Man, H. Y. Su, F. Calle-Vallejo, H. A. Hansen, J. I. Martinez, N. G. Inoglu, J. Kitchin, T. F. Jaramillo, J. K. Norskov, J. Rossmeisl, *ChemCatChem* **2011**, *3*, 1159.
[43] H. Ibrahim, A. Ilinca, J. Perron, *Renewable Sustainable Energy Rev.* **2008**, *12*, 1221.
[44] H. S. Casalongue, S. Kaya, V. Viswanathan, D. J. Miller, D. Friebel, H. A. Hansen, J. K. Nørskov, A. Nilsson, H. Ogasawara, *Nat. Commun.* **2013**, *4*, 2817.
[45] Y. Matsumoto, E. Sato, *Mater. Chem. Phys.* **1986**, *14*, 397.
[46] M.-R. Gao, Y.-F. Xu, J. Jiang, S.-H. Yu, *Chem. Soc. Rev.* **2013**, *42*, 2986.
[47] E. Fabbri, A. Habereder, K. Waltar, R. Kotz, T. J. Schmidt, *Catal. Sci. Technol.* **2014**, *4*, 3800.
[48] Y. Jiao, Y. Zheng, M. Jaroniec, S. Z. Qiao, *Chem. Soc. Rev.* **2015**, *44*, 2060.
[49] P. C. K. Vesborg, B. Seger, I. Chorkendorff, *J. Phys. Chem. Lett.* **2015**, *6*, 951.
[50] J. Durst, A. Siebel, C. Simon, F. Hasché, J. Herranz, H. A. Gasteiger, *Energy Environ. Sci.* **2014**, *7*, 2255.
[51] B. E. Conway, G. Jerkiewicz, *Solid State Ionics* **2002**, *150*, 93.
[52] B. E. Conway, B. V. Tilak, *Electrochim. Acta* **2002**, *47*, 3571.
[53] Y. Shi, B. Zhang, *Chem. Soc. Rev.* **2016**, *45*, 1529.
[54] B. Hinnemann, P. G. Moses, J. Bonde, K. P. Jørgensen, J. H. Nielsen, S. Horch, I. Chorkendorff, J. K. Nørskov, *J. Am. Chem. Soc.* **2005**, *127*, 5308.
[55] J.O'M. Bockris, *J. Chem. Phys.* **1956**, *24*, 817.
[56] A. I. Krasil'shchkov, *Zh. Fiz. Khim.* **1963**, *37*, 273.
[57] W. H. Wade, N. Hackerman, *Trans. Faraday Soc.* **1957**, *53*, 1636.
[58] W. E. O'Grady, C. Iwakura, J. Huang, E. Yeager, in *Proc. Symp. on Electrocatalysis* (Ed: M. W. Breiter), The Electrochemical Society, Princeton, NJ **1974**, p. 286.
[59] W. O'Grady, C. Iwakura, E. Yeager, *Am. Soc. Mech. Eng.* **1976**, *76-ENAs-37*, 1.
[60] J. O'M. Bockris, T. Otagawa, *J. Electrochem. Soc.* **1984**, *131*, 290.
[61] B. E. Conway, M. Salomon, *Electrochim. Acta* **1964**, *9*, 1599.
[62] R. L. Doyle, M. E. G. Lyons, in *Photoelectrochemical Solar Fuel Production: From Basic Principles to Advanced Devices* (Eds: S. Giménez, J. Bisquert), Springer International Publishing, Cham, Switzerland **2016**, p. 41.

[63] J. Rossmeisl, Z. W. Qu, H. Zhu, G. J. Kroes, J. K. Nørskov, *J. Electroanal. Chem.* **2007**, *607*, 83.
[64] H. Dau, C. Limberg, T. Reier, M. Risch, S. Roggan, P. Strasser, *ChemCatChem* **2010**, *2*, 724.
[65] Y. Pan, Y. Liu, J. Zhao, K. Yang, J. Liang, D. Liu, W. Hu, D. Liu, Y. Liu, C. Liu, *J. Mater. Chem. A* **2015**, *3*, 1656.
[66] J. F. Callejas, C. G. Read, E. J. Popczun, J. M. McEnaney, R. E. Schaak, *Chem. Mater.* **2015**, *27*, 3769.
[67] P. Liu, J. A. Rodriguez, *J. Am. Chem. Soc.* **2005**, *127*, 14871.
[68] P. Xiao, M. A. Sk, L. Thia, X. M. Ge, R. J. Lim, J. Y. Wang, K. H. Lim, X. Wang, *Energy Environ. Sci.* **2014**, *7*, 2624.
[69] H. Li, C. Tsai, A. L. Koh, L. Cai, A. W. Contryman, A. H. Fragapane, J. Zhao, H. S. Han, H. C. Manoharan, F. Abild-Pedersen, J. K. Nørskov, X. Zheng, *Nat. Mater.* **2016**, *15*, 48.
[70] M. Zeng, Y. Li, *J. Mater. Chem. A* **2015**, *3*, 14942.
[71] J. Wang, J. Liu, B. Zhang, X. Ji, K. Xu, C. Chen, L. Miao, J. Jiang, *Phys. Chem. Chem. Phys.* **2017**, *19*, 10125.
[72] Y. Yin, J. Han, Y. Zhang, X. Zhang, P. Xu, Q. Yuan, L. Samad, X. Wang, Y. Wang, Z. Zhang, P. Zhang, X. Cao, B. Song, S. Jin, *J. Am. Chem. Soc.* **2016**, *138*, 7965.
[73] J. Staszak-Jirkovský, C. D. Malliakas, P. P. Lopes, N. Danilovic, S. S. Kota, K.-C. Chang, B. Genorio, D. Strmcnik, V. R. Stamenkovic, M. G. Kanatzidis, N. M. Markovic, *Nat. Mater.* **2016**, *15*, 197.
[74] R. Subbaraman, D. Tripkovic, K.-C. Chang, D. Strmcnik, A. P. Paulikas, P. Hirunsit, M. Chan, J. Greeley, V. Stamenkovic, N. M. Markovic, *Nat. Mater.* **2012**, *11*, 550.
[75] W. Chen, H. Wang, Y. Li, Y. Liu, J. Sun, S. Lee, J.-S. Lee, Y. Cui, *ACS Cent. Sci.* **2015**, *1*, 244.
[76] O. Mabayoje, A. Shoola, B. R. Wygant, C. B. Mullins, *ACS Energy Lett.* **2016**, *1*, 195.
[77] J. Ryu, N. Jung, J. H. Jang, H.-J. Kim, S. J. Yoo, *ACS Catal.* **2015**, *5*, 4066.
[78] L.-A. Stern, L. Feng, F. Song, X. Hu, *Energy Environ. Sci.* **2015**, *8*, 2347.
[79] A. Dutta, A. K. Samantara, S. K. Dutta, B. K. Jena, N. Pradhan, *ACS Energy Lett.* **2016**, *1*, 169.
[80] Y. Yin, R. M. Rioux, C. K. Erdonmez, S. Hughes, G. A. Somorjai, A. P. Alivisatos, *Science* **2004**, *304*, 711.
[81] B. You, N. Jiang, M. Sheng, Y. Sun, *Chem. Commun.* **2015**, *51*, 4252.
[82] Y. Feng, C. Xu, E. Hu, B. Xia, J. Ning, C. Zheng, Y. Zhong, Z. Zhang, Y. Hu, *J. Mater. Chem. A* **2018**, *6*, 14103.
[83] Y. Jiang, X. Qian, C. Zhu, H. Liu, L. Hou, *ACS Appl. Mater. Interfaces* **2018**, *10*, 9379.
[84] B. Zhang, G. Yang, C. Li, K. Huang, J. Wu, S. Hao, J. Feng, D. Peng, Y. Huang, *Nanoscale* **2018**, *10*, 1774.
[85] H. Sun, X. Xu, Z. Yan, X. Chen, F. Cheng, P. S. Weiss, J. Chen, *Chem. Mater.* **2017**, *29*, 8539.
[86] Z. Yin, C. Zhu, C. Li, S. Zhang, X. Zhang, Y. Chen, *Nanoscale* **2016**, *8*, 19129.
[87] H. Zhang, L. V. Solomon, D.-H. Ha, S. Honrao, R. G. Hennig, R. D. Robinson, *Dalton Trans.* **2013**, *42*, 12596.
[88] J. Kim, H. Jin, A. Oh, H. Baik, S. H. Joo, K. Lee, *Nanoscale* **2017**, *9*, 15397.
[89] J. Xu, J. Cui, C. Guo, Z. Zhao, R. Jiang, S. Xu, Z. Zhuang, Y. Huang, L. Wang, Y. Li, *Angew. Chem., Int. Ed.* **2016**, *55*, 6502.
[90] V. Ganesan, P. Ramasamy, J. Kim, *Int. J. Hydrogen Energy* **2017**, *42*, 5985.
[91] Z. Yu, Y. Bai, S. Zhang, Y. Liu, N. Zhang, K. Sun, *Int. J. Hydrogen Energy* **2018**, *43*, 8815.
[92] B. You, N. Jiang, M. Sheng, S. Gul, J. Yano, Y. Sun, *Chem. Mater.* **2015**, *27*, 7636.
[93] Y. Li, J. Liu, C. Chen, X. Zhang, J. Chen, *ACS Appl. Mater. Interfaces* **2017**, *9*, 5982.
[94] Y. Guo, J. Tang, H. Qian, Z. Wang, Y. Yamauchi, *Chem. Mater.* **2017**, *29*, 5566.
[95] P. He, X.-Y. Yu, X. W. Lou, *Angew. Chem., Int. Ed.* **2017**, *56*, 3897.
[96] B. Y. Guan, L. Yu, X. W. Lou, *Angew. Chem., Int. Ed.* **2017**, *56*, 2386.
[97] W. Wang, B. Jiang, C. Qian, F. Lv, J. Feng, J. Zhou, K. Wang, C. Yang, Y. Yang, S. Guo, *Adv. Mater.* **2018**, *30*, 1801812.
[98] Y. Yang, M. Luo, Y. Xing, S. Wang, W. Zhang, F. Lv, Y. Li, Y. Zhang, W. Wang, S. Guo, *Adv. Mater.* **2018**, *30*, 1706085.
[99] L. Zhang, H. B. Wu, X. W. Lou, *J. Am. Chem. Soc.* **2013**, *135*, 10664.
[100] T. Kim, J. Park, H. Jin, A. Oh, H. Baik, S. H. Joo, K. Lee, *Nanoscale* **2018**, *10*, 9845.
[101] Z. Zhao, D. E. Schipper, A. P. Leitner, H. Thirumalai, J.-H. Chen, L. Xie, F. Qin, M. K. Alam, L. C. Grabow, S. Chen, D. Wang, Z. Ren, Z. Wang, K. H. Whitmire, J. Bao, *Nano Energy* **2017**, *39*, 444.
[102] H. Wang, Y. Xie, H. Cao, Y. Li, L. Li, Z. Xu, X. Wang, N. Xiong, K. Pan, *ChemSusChem* **2017**, *10*, 4899.
[103] J. Jiang, S. Lu, H. Gao, X. Zhang, H.-Q. Yu, *Nano Energy* **2016**, *27*, 526.
[104] E. H. Robinson, M. J. Turo, J. E. Macdonald, *Chem. Mater.* **2017**, *29*, 3854.
[105] L. An, L. Huang, H. Liu, P. Xi, F. Chen, Y. Du, *Part. Part. Syst. Charact.* **2015**, *32*, 536.
[106] D. Yoon, H. Jin, S. Ryu, S. Park, H. Baik, S. J. Oh, S. Haam, C. Joo, K. Lee, *CrystEngComm* **2015**, *17*, 4627.
[107] E. J. Popczun, C. W. Roske, C. G. Read, J. C. Crompton, J. M. McEnaney, J. F. Callejas, N. S. Lewis, R. E. Schaak, *J. Mater. Chem. A* **2015**, *3*, 5420.
[108] B. Seo, D. S. Baek, Y. J. Sa, S. H. Joo, *CrystEngComm* **2016**, *18*, 6083.
[109] J. B. Rivest, P. K. Jain, *Chem. Soc. Rev.* **2013**, *42*, 89.
[110] J. Park, J. Park, J. Lee, A. Oh, H. Baik, K. Lee, *ACS Nano* **2018**, *12*, 7996.
[111] Q. Yuan, D. Liu, N. Zhang, W. Ye, H. Ju, L. Shi, R. Long, J. Zhu, Y. Xiong, *Angew. Chem.* **2017**, *129*, 4270.
[112] L. De Trizio, R. Gaspari, G. Bertoni, I. Kriegel, L. Moretti, F. Scotognella, L. Maserati, Y. Zhang, G. C. Messina, M. Prato, S. Marras, A. Cavalli, L. Manna, *Chem. Mater.* **2015**, *27*, 1120.
[113] H.-L. Wu, R. Sato, A. Yamaguchi, M. Kimura, M. Haruta, H. Kurata, T. Teranishi, *Science* **2016**, *351*, 1306.
[114] J. Joo, H. Jin, A. Oh, B. Kim, J. Lee, H. Baik, S. H. Joo, K. Lee, *J. Mater. Chem. A* **2018**, *6*, 16130.
[115] G. Prieto, H. Tüysüz, N. Duyckaerts, J. Knossalla, G.-H. Wang, F. Schüth, *Chem. Rev.* **2016**, *116*, 14056.
[116] C. Zhang, Y. Huang, Y. Yu, J. Zhang, S. Zhuo, B. Zhang, *Chem. Sci.* **2017**, *8*, 2769.
[117] G. Hu, Q. Tang, D.-E. Jiang, *Phys. Chem. Chem. Phys.* **2016**, *18*, 23864.
[118] S. Jin, *ACS Energy Lett.* **2017**, *2*, 1937.
[119] H. Kakizaki, H. Ooka, T. Hayashi, A. Yamaguchi, N. Bonnet-Mercier, K. Hashimoto, R. Nakamura, *Adv. Funct. Mater.* **2018**, *28*, 1706319.
[120] Y. Yan, B. Y. Xia, X. Ge, Z. Liu, A. Fisher, X. Wang, *Chem. - Eur. J.* **2015**, *21*, 18062.
[121] F. Hu, S. Zhu, S. Chen, Y. Li, L. Ma, T. Wu, Y. Zhang, C. Wang, C. Liu, X. Yang, L. Song, X. Yang, Y. Xiong, *Adv. Mater.* **2017**, *29*, 1606570.
[122] Q. Liu, Z. H. Pu, A. M. Asiri, X. P. Sun, *Electrochim. Acta* **2014**, *149*, 324.
[123] T.-W. Lin, C.-J. Liu, C.-S. Dai, *Appl. Catal., B* **2014**, *154–155*, 213.
[124] Z. Xing, Q. Liu, A. M. Asiri, X. Sun, *Adv. Mater.* **2014**, *26*, 5702.
[125] B. Guo, K. Yu, H. Li, H. Song, Y. Zhang, X. Lei, H. Fu, Y. Tan, Z. Zhu, *ACS Appl. Mater. Interfaces* **2016**, *8*, 5517.
[126] D. Zhou, L. He, W. Zhu, X. Hou, K. Wang, G. Du, C. Zheng, X. Sun, A. M. Asiri, *J. Mater. Chem. A* **2016**, *4*, 10114.

[127] J. Wu, M. Liu, K. Chatterjee, K. P. Hackenberg, J. Shen, X. Zou, Y. Yan, J. Gu, Y. Yang, J. Lou, P. M. Ajayan, *Adv. Mater. Interfaces* **2016**, *3*, 1500669.
[128] H. Li, Y. Shao, Y. Su, Y. Gao, X. Wang, *Chem. Mater.* **2016**, *28*, 1155.
[129] C.-C. Hou, S. Cao, W.-F. Fu, Y. Chen, *ACS Appl. Mater. Interfaces* **2015**, *7*, 28412.
[130] A. M. Wiltrout, C. G. Read, E. M. Spencer, R. E. Schaak, *Inorg. Chem.* **2016**, *55*, 221.
[131] K. Liu, C. Zhang, Y. Sun, G. Zhang, X. Shen, F. Zou, H. Zhang, Z. Wu, E. C. Wegener, C. J. Taubert, J. T. Miller, Z. Peng, Y. Zhu, *ACS Nano* **2018**, *12*, 158.
[132] H. Lei, M. Chen, Z. Liang, C. Liu, W. Zhang, R. Cao, *Catal. Sci. Technol.* **2018**, *8*, 2289.
[133] H.-H. Zou, C.-Z. Yuan, H.-Y. Zou, T.-Y. Cheang, S.-J. Zhao, U. Y. Qazi, S.-L. Zhong, L. Wang, A.-W. Xu, *Catal. Sci. Technol.* **2017**, *7*, 1549.
[134] Q. Xiong, X. Zhang, H. Wang, G. Liu, G. Wang, H. Zhang, H. Zhao, *Chem. Commun.* **2018**, *54*, 3859.
[135] L. Yu, B. Y. Xia, X. Wang, X. W. Lou, *Adv. Mater.* **2016**, *28*, 92.
[136] Y. Liu, C. Xiao, M. Lyu, Y. Lin, W. Cai, P. Huang, W. Tong, Y. Zou, Y. Xie, *Angew. Chem.* **2015**, *127*, 11383.
[137] P. Ganesan, M. Prabu, J. Sanetuntikul, S. Shanmugam, *ACS Catal.* **2015**, *5*, 3625.